J. Fluid Mech. (1992), *vol.* 238, *pp.* 155–185
Printed in Great Britain

Toward the large-eddy simulation of compressible turbulent flows

By G. ERLEBACHER[1], M. Y. HUSSAINI[1], C. G. SPEZIALE[1]
AND T. A. ZANG[2]

[1] ICASE, NASA Langley Research Center, Hampton, VA 23665, USA
[2] NASA Langley Research Center, Hampton, VA 23665, USA

(Received 16 October 1990 and in revised form 30 September 1991)

New subgrid-scale models for the large-eddy simulation of compressible turbulent flows are developed and tested based on the Favre-filtered equations of motion for an ideal gas. A compressible generalization of the linear combination of the Smagorinsky model and scale-similarity model, in terms of Favre-filtered fields, is obtained for the subgrid-scale stress tensor. An analogous thermal linear combination model is also developed for the subgrid-scale heat flux vector. The two dimensionless constants associated with these subgrid-scale models are obtained by correlating with the results of direct numerical simulations of compressible isotropic turbulence performed on a 96^3 grid using Fourier collocation methods. Extensive comparisons between the direct and modelled subgrid-scale fields are provided in order to validate the models. A large-eddy simulation of the decay of compressible isotropic turbulence – conducted on a coarse 32^3 grid – is shown to yield results that are in excellent agreement with the fine-grid direct simulation. Future applications of these compressible subgrid-scale models to the large-eddy simulation of more complex supersonic flows are discussed briefly.

1. Introduction

The direct numerical simulation of turbulent flows at the high Reynolds numbers encountered in problems of technological importance is all but impossible as a result of the wide range of scales that are present. Consequently, the solutions to such problems must invariably be based on some form of turbulence modelling. Traditional turbulence models based on Reynolds averages have had only limited success since the large scales of the turbulence – which contain most of the energy – are highly dependent on the geometry of the flow being considered. Experience has indicated that such models usually break down when a variety of turbulent flows are considered (Lumley 1983). The small scales are more universal in character, and serve mainly as a source for dissipation. Hence, it can be argued that a better understanding of turbulent flows could be achieved if just the small scales are modelled while the large scales are calculated (Deardorff 1970). This is the fundamental idea behind large-eddy simulations.

During the past decade, considerable progress has been made in the large-eddy simulation of incompressible turbulent flows. This effort has shed new light on the physics of turbulence. The earliest work relied heavily on the use of the Reynolds averaging assumption to eliminate the Leonard and cross-stresses while the Reynolds stresses were computed using the Smagorinsky model (Deardorff 1970; Leonard 1974; Reynolds 1976). More recent large-eddy simulations have been based on the direct calculation of the Leonard stresses with models provided for the cross- and Reynolds subgrid-scale stresses in order to enhance the numerical accuracy (see Biringen & Reynolds 1981; Bardina, Ferziger & Reynolds 1983). However, among these newer models, only the Bardina *et al.* (1983) model, with a Bardina constant of 1.0, satisfies the important physical constraint of Galilean invariance (Speziale 1985). The underlying physical concepts, fundamental numerical algorithms, and comprehensive historical data behind the recent field of large-eddy simulation have been presented in articles by Schumann (1975), Voke & Collins (1983) and Rogallo & Moin (1984). More recently, work on the subgrid-scale modelling of transition to turbulence of initially laminar incompressible flows has begun (Piomelli *et al.* 1990). Several large-eddy simulations have been performed and initial results are promising.

Despite the intensive research effort that has been devoted to the large-eddy simulation of incompressible flows as outlined above, it appears that no full large-eddy simulation of a compressible turbulent flow has yet been attempted. Of course, such work could have important technological applications in the analysis of turbulent supersonic flows, where shock waves are generated, and in turbulent flows within combustion chambers. The prerequisite for carrying out such computations is the development of suitable subgrid-scale models for compressible turbulent flows. With the exception of the recent work of Yoshizawa (1986) and Speziale *et al.* (1988), few, if any, studies along these lines appear to have been published. The subgrid-scale models of Yoshizawa are only suitable for slightly compressible turbulent flows since they made use of an asymptotic expansion about an incompressible state. Recently however, Zang, Dahlburg & Dahlburg (1992) have performed an extensive parameter study using the model developed by Speziale *et al.* (1988). It was shown by Speziale *et al.* (1988) that, for accuracy, the Leonard and cross-stresses must be accounted for. Furthermore, the modelling of the isotropic part of the Reynolds subgrid-scale stress tensor was shown to be questionable – an issue that was left for future research.

In this paper, complete subgrid-scale models are developed for the closure of the Favre-filtered Navier–Stokes and energy equations. The compressible subgrid-scale stress model that is obtained in §2 reduces to the linear combination model of Bardina *et al.* (1983) in the incompressible limit. Likewise, the subgrid-scale heat flux model that is obtained herein consists of an analogous linear combination of scale similarity and gradient transport terms. The dimensionless constant which appears in the subgrid-scale stress model is arrived at through correlation analysis of data generated from direct numerical simulations of compressible isotropic turbulence. A more detailed comparison of computed and modelled subgrid-scale fields is presented along with the results of a large-eddy simulation of compressible isotropic turbulence.

2. Subgrid-scale models for compressible turbulence

The compressible turbulent flow of an ideal gas is considered. Such flows are governed by the continuity, momentum and energy equations which – neglecting body forces – are given by (cf. Batchelor 1967)

$$\frac{\partial \rho}{\partial t}+\frac{\partial(\rho v_k)}{\partial x_k}=0, \tag{1}$$

$$\frac{\partial(\rho v_k)}{\partial t}+\frac{\partial(\rho v_k v_l)}{\partial x_l}=-\frac{\partial p}{\partial x_k}+\frac{\partial \sigma_{kl}}{\partial x_l}, \tag{2}$$

$$\frac{\partial(\rho h)}{\partial t}+\frac{\partial(\rho h v_k)}{\partial x_k}=\frac{\partial p}{\partial t}+v_k\frac{\partial p}{\partial x_k}+\frac{\partial}{\partial x_k}\left(\kappa\frac{\partial T}{\partial x_k}\right)+\Phi, \tag{3}$$

respectively, where ρ is the mass density, $\boldsymbol{v}$ is the velocity vector, p is the thermodynamic pressure, μ is the dynamic viscosity, h is the enthalpy, T is the absolute temperature, and κ is the thermal conductivity. The viscous stress σ_{kl} and the viscous dissipation Φ are defined by

$$\sigma_{kl}=-\tfrac{2}{3}\mu\frac{\partial v_j}{\partial x_j}\delta_{kl}+\mu\left(\frac{\partial v_k}{\partial x_l}+\frac{\partial v_l}{\partial x_k}\right), \tag{4}$$

$$\Phi=-\tfrac{2}{3}\mu\left(\frac{\partial v_j}{\partial x_j}\right)^2+\mu\left(\frac{\partial v_k}{\partial x_l}+\frac{\partial v_l}{\partial x_k}\right)\frac{\partial v_k}{\partial x_l}, \tag{5}$$

respectively. Herein, the Einstein summation convention applies to repeated indices. Equations (1)–(3) must be supplemented with the equations of state

$$p=\rho RT, \quad h=C_p T \tag{6}$$

for an ideal gas where R is the ideal gas constant and C_p is the specific heat at constant pressure. Likewise, the dependence of the viscosity and thermal conductivity on the temperature must be provided (i.e. relationships of the form $\mu=\mu(T)$ and $\kappa=\kappa(T)$ are needed and these depend on the gas under consideration).

Any flow variable $\mathscr{F}$ can be filtered in the following manner:

$$\bar{\mathscr{F}}(\boldsymbol{x})=\int_D G(\boldsymbol{x}-\boldsymbol{z},\Delta)\ \mathscr{F}(\boldsymbol{z})\,\mathrm{d}^3z, \tag{7}$$

where G is a filter function, Δ is the computational mesh size, and D is the domain of the fluid. The filter function G is typically taken to be an infinitely differentiable function of bounded support in a compact domain, or a Gaussian distribution in a periodic domain. (A Gaussian filter is adopted for the calculations in this study.) The filter-function is normalized by requiring that

$$\int_D G(\boldsymbol{x}-\boldsymbol{z},\Delta)\,\mathrm{d}^3z=1. \tag{8}$$

It follows that, in the limit as the computational mesh size goes to zero, (7) becomes a Dirac delta sequence, i.e.

$$\lim_{\Delta\to 0}\int_D G(\boldsymbol{x}-\boldsymbol{z},\Delta)\mathscr{F}(\boldsymbol{z})\,\mathrm{d}^3z=\int_D \delta(\boldsymbol{x}-\boldsymbol{z})\mathscr{F}(\boldsymbol{z})\,\mathrm{d}^3z=\mathscr{F}(\boldsymbol{x}), \tag{9}$$

where $\delta(\boldsymbol{x}-\boldsymbol{z})$ is the Dirac delta function (Arfken 1970). The filter function has the property that the amplitudes of the high-frequency spatial Fourier components of any flow variable $\mathscr{F}$ are substantially reduced. Consequently, $\bar{\mathscr{F}}$ represents the large-scale part of $\mathscr{F}$. At this point, it should be mentioned that as a result of the defining properties of G, it follows that

$$\overline{\frac{\partial\mathscr{F}}{\partial t}}=\frac{\partial\bar{\mathscr{F}}}{\partial t}, \quad \overline{\frac{\partial\mathscr{F}}{\partial x_k}}=\frac{\partial\bar{\mathscr{F}}}{\partial x_k}. \tag{10}$$

Piomelli, Ferziger & Moin (1987) discuss the relationship between the form of the filter function and that of the subgrid-scale turbulence model.

The turbulent fields are decomposed as follows, based on Favre filtering:

$$\mathscr{F} = \tilde{\mathscr{F}} + \mathscr{F}', \tag{11}$$

where the Favre filter

$$\tilde{\mathscr{F}} = \frac{\overline{\rho \mathscr{F}}}{\bar{\rho}} \tag{12}$$

is defined in an analogous manner to the Favre time average which has been used in the more traditional studies of compressible turbulent flows (Hinze 1975). However, contrary to the more traditional Favre time averaging,

$$\tilde{\tilde{\mathscr{F}}} \neq \tilde{\mathscr{F}} \tag{13}$$

in general, and hence

$$\tilde{\mathscr{F}}' \neq 0. \tag{14}$$

The direct filtering of the continuity equation (1) yields

$$\frac{\partial \bar{\rho}}{\partial t} + \frac{\partial (\bar{\rho} \tilde{v}_k)}{\partial x_k} = 0, \tag{15}$$

where we have used (10) and (12). Likewise, a direct filtering of the momentum equation yields

$$\frac{\partial (\bar{\rho} \tilde{v}_k)}{\partial t} + \frac{\partial (\bar{\rho} \tilde{v}_k \tilde{v}_l)}{\partial x_l} = -\frac{\partial \bar{p}}{\partial x_k} + \frac{\partial \bar{\sigma}_{kl}}{\partial x_l} + \frac{\partial \tau_{kl}}{\partial x_l}, \tag{16}$$

where

$$\bar{p} = \bar{\rho} R \tilde{T} \tag{17}$$

and

$$\tau_{kl} = -\bar{\rho}(\widetilde{\tilde{v}_k \tilde{v}_l} - \tilde{v}_k \tilde{v}_l + \widetilde{v'_k \tilde{v}_l} + \widetilde{v'_l \tilde{v}_k} + \widetilde{v'_k v'_l}) \tag{18}$$

is the subgrid-scale stress tensor. The subgrid-scale stress tensor can be decomposed as follows:

$$\boldsymbol{\tau} = \boldsymbol{L} + \boldsymbol{C} + \boldsymbol{R} \tag{19}$$

where

$$L_{kl} = -\bar{\rho}(\widetilde{\tilde{v}_k \tilde{v}_l} - \tilde{v}_k \tilde{v}_l), \tag{20}$$

$$C_{kl} = -\bar{\rho}(\widetilde{v'_k \tilde{v}_l} + \widetilde{v'_l \tilde{v}_k}), \tag{21}$$

$$R_{kl} = -\bar{\rho}\widetilde{v'_k v'_l} \tag{22}$$

are respectively, the subgrid-scale Leonard, cross-, and Reynolds stresses based on Favre filtering. From (20), it is clear that the Leonard stress can be calculated directly and does not need to be modelled. The cross-stress is modelled with the scale similarity model

$$C_{kl} = -\bar{\rho}(\tilde{v}_k \tilde{v}_l - \tilde{\tilde{v}}_k \tilde{\tilde{v}}_l) \tag{23}$$

(with a coefficient of unity to ensure Galilean invariance of the overall model). This model is analogous to its incompressible counterpart, which has been reasonably successful in the large-eddy simulation of incompressible turbulent flows (Bardina *et al.* 1983; Speziale 1985). The subgrid-scale Reynolds stress tensor is separated into deviatoric and isotropic parts, respectively, as follows:

$$\boldsymbol{R} = {}_{\mathrm{D}}\boldsymbol{R} + {}_{\mathrm{I}}\boldsymbol{R}, \tag{24}$$

where

$${}_{\mathrm{D}}R_{kl} = -\bar{\rho}(\widetilde{v'_k v'_l} - \tfrac{1}{3}\widetilde{v'_i v'_i}\delta_{kl}), \tag{25}$$

and

$${}_{\mathrm{I}}R_{kl} = -\tfrac{1}{3}\bar{\rho}\widetilde{v'_i v'_i}\delta_{kl}. \tag{26}$$

The deviatoric part of the subgrid-scale Reynolds stress tensor, ${}_{\mathrm{D}}\boldsymbol{R}$, is modelled using the compressible generalization of the Smagorinsky model that is given by

$$ {}_{\mathrm{D}}R_{kl} = 2C_R\bar{\rho}\Delta^2\mathrm{II}_{\tilde{S}}^{\frac{1}{2}}(\tilde{S}_{kl}-\tfrac{1}{3}\tilde{S}_{mm}\,\delta_{kl}), \tag{27}$$

where

$$\tilde{S}_{kl} = \frac{1}{2}\left(\frac{\partial\tilde{v}_k}{\partial x_l}+\frac{\partial\tilde{v}_l}{\partial x_k}\right), \tag{28}$$

$$\mathrm{II}_{\tilde{S}} = \tilde{S}_{mn}\tilde{S}_{mn} \tag{29}$$

(i.e. $\tilde{\boldsymbol{S}}$ is the Favre-filtered rate of strain tensor while $\mathrm{II}_{\tilde{S}}$ is its second invariant) and C_R is the compressible Smagorinsky constant. Yoshizawa – by means of a two-scale DIA method – derived a model for the isotropic part of the subgrid-scale Reynolds stress tensor, ${}_{\mathrm{I}}\boldsymbol{R}$, given by

$${}_{\mathrm{I}}R_{kl} = -\tfrac{2}{3}C_{\mathrm{I}}\bar{\rho}\Delta^2\mathrm{II}_{\tilde{S}}\,\delta_{kl}, \tag{30}$$

where C_{I} is a dimensionless constant. Equation (30) can, for the most part, be obtained from a turbulence production equals dissipation equilibrium hypothesis (Yoshizawa 1986). However, this model was shown by Speziale *et al.* (1988) to correlate very poorly with the results of direct numerical simulations of compressible isotropic turbulence. Since ${}_{\mathrm{I}}R_{kl} = -\frac{1}{3}\bar{\rho}q^2_{\mathrm{SGS}}\,\delta_{kl}$, this term only appears in the filtered equations of motion, coupled with the thermodynamic pressure, through the term $-\nabla(\bar{p}+\frac{1}{3}\bar{\rho}q^2_{\mathrm{SGS}})$. However, it follows that

$$\begin{aligned}\frac{1}{3}\frac{\bar{\rho}q^2_{\mathrm{SGS}}}{\bar{p}} &= \frac{1}{3}\frac{q^2_{\mathrm{SGS}}}{R\tilde{T}}\\ &= \tfrac{1}{3}\gamma M^2_{\mathrm{SGS}},\end{aligned}$$

where $M_{\mathrm{SGS}} = [q^2_{\mathrm{SGS}}/(\gamma R\tilde{T})]^{\frac{1}{2}}$ is the subgrid-scale turbulence Mach number and $\gamma = C_p/C_v$ is the ratio of specific heats. For $M_{\mathrm{SGS}} < 0.4$, the isotropic part of the subgrid-scale stress tensor is dominated by the thermodynamic pressure. Consequently, since the subgrid-scale turbulence Mach number is generally less than the local turbulence Mach number M_{t} – and since turbulence Mach numbers $M_{\mathrm{t}} > 0.6$ are not commonly encountered – we believe that ${}_{\mathrm{I}}R_{kl}$ can be neglected in most compressible turbulent flows without introducing appreciable errors. This assumption is validated later by direct numerical simulations. Hence, the overall subgrid-scale stress model we propose takes the form

$$\tau_{kl} = -\bar{\rho}(\widetilde{\tilde{v}_k\tilde{v}_l}-\tilde{\tilde{v}}_k\tilde{\tilde{v}}_l)+2C_R\bar{\rho}\Delta^2\mathrm{II}_{\tilde{S}}^{\frac{1}{2}}(\tilde{S}_{kl}-\tfrac{1}{3}\tilde{S}_{mm}\,\delta_{kl}). \tag{31}$$

In the incompressible limit, (31) reduces to the linear combination model,

$$-\tau_{kl}/\rho = \overline{\bar{v}_k\bar{v}_l}-\bar{\bar{v}}_k\bar{\bar{v}}_l-2C_R\Delta^2\mathrm{II}_{\bar{S}}^{\frac{1}{2}}\bar{S}_{kl}, \tag{32}$$

of Bardina *et al.* (1983), where the Bardina constant is one in order to satisfy Galilean invariance. This reduction process is a consequence of (31) and the fact that

$$\tilde{\boldsymbol{v}} = \bar{\boldsymbol{v}}, \quad \tilde{S}_{mm} = \bar{S}_{mm} = 0 \tag{33}$$

when ρ becomes constant.

A direct filtering of the energy equation yields the filtered form

$$\frac{\partial(C_p\bar{\rho}\tilde{T})}{\partial t}+\frac{\partial(C_p\bar{\rho}\tilde{v}_k\tilde{T})}{\partial x_k} = \frac{\partial\bar{p}}{\partial t}+\overline{v_k\frac{\partial p}{\partial x_k}}+\bar{\Phi}+\frac{\partial}{\partial x_k}\overline{\left(\kappa\frac{\partial T}{\partial x_k}\right)}-\frac{\partial Q_k}{\partial x_k}, \tag{34}$$

where
$$Q_k = C_p\bar{\rho}(\widetilde{\tilde{v}_k\tilde{T}}-\tilde{v}_k\tilde{T}+\widetilde{v'_k\tilde{T}}+\widetilde{\tilde{v}_k T'}+\widetilde{v'_k T'}) \tag{35}$$

is the subgrid-scale heat flux. The subgrid-scale heat flux can be decomposed in the same fashion as the subgrid-scale stresses. This leads to

$$\boldsymbol{Q} = \boldsymbol{Q}^{(\mathrm{L})}+\boldsymbol{Q}^{(\mathrm{C})}+\boldsymbol{Q}^{(\mathrm{R})} \tag{36}$$

where
$$Q_k^{(\mathrm{L})} = C_p\bar{\rho}(\widetilde{\tilde{v}_k\tilde{T}}-\tilde{v}_k\tilde{T}), \tag{37}$$
$$Q_k^{(\mathrm{C})} = C_p\bar{\rho}(\widetilde{v'_k\tilde{T}}+\widetilde{\tilde{v}_k T'}), \tag{38}$$
$$Q_k^{(\mathrm{R})} = C_p\bar{\rho}\widetilde{v'_k T'} \tag{39}$$

are the Leonard, cross-, and Reynolds heat fluxes. Analogous to the modelling of the cross-stress, the cross-heat flux is modelled using the scale similarity format

$$Q_k^{(\mathrm{C})} = C_p\bar{\rho}(\tilde{v}_k\tilde{T}-\tilde{\tilde{v}}_k\tilde{\tilde{T}}). \tag{40}$$

The Reynolds heat flux is modelled with the usual gradient transport hypothesis as follows (cf. Eidson 1985):

$$\widetilde{v'_k T'} = -\frac{C_R}{Pr_{\mathrm{T}}}\Delta^2\mathrm{II}_{\tilde{S}}^{\frac{1}{2}}\frac{\partial\tilde{T}}{\partial x_k}, \tag{41}$$

where Pr_{T} is the turbulent Prandtl number. Of course, the Leonard heat flux can be calculated directly. Hence, the overall model for the subgrid-scale heat flux we propose is as follows:

$$Q_k = C_p\bar{\rho}\left[(\widetilde{\tilde{v}_k\tilde{T}}-\tilde{\tilde{v}}_k\tilde{\tilde{T}})-\frac{C_R}{Pr_{\mathrm{T}}}\Delta^2\mathrm{II}_{\tilde{S}}^{\frac{1}{2}}\frac{\partial\tilde{T}}{\partial x_k}\right], \tag{42}$$

and is obtained by combining (37), (40), and (41).

At this point, some comments need to be made concerning the viscous terms on the right-hand side of (16) and the pressure gradient–velocity and viscous dissipation terms which appear on the right-hand side of (34). The pressure gradient–velocity correlation can be written in the alternative form

$$\begin{aligned}\overline{v_k\frac{\partial p}{\partial x_k}} &= \frac{\partial(\overline{pv_k})}{\partial x_k}-\overline{p\frac{\partial v_k}{\partial x_k}}\\ &= \frac{\partial}{\partial x_k}(\overline{\rho RTv_k})-\overline{p\frac{\partial v_k}{\partial x_k}}\\ &= \frac{\partial}{\partial x_k}(\bar{\rho}R\tilde{v}_k\tilde{T})+\frac{\partial}{\partial x_k}\left(\frac{R}{C_p}Q_k\right)-\overline{p\frac{\partial v_k}{\partial x_k}},\end{aligned} \tag{43}$$

where only the pressure dilatation term

$$\begin{aligned}\overline{p\frac{\partial v_k}{\partial x_k}} &= \bar{\rho}R\left(\widetilde{T\frac{\partial v_k}{\partial x_k}}\right)\\ &= \bar{\rho}R\widetilde{\tilde{T}\frac{\partial\tilde{v}_k}{\partial x_k}}+\bar{\rho}R\widetilde{T'\frac{\partial\tilde{v}_k}{\partial x_k}}+\bar{\rho}R\widetilde{\tilde{T}\frac{\partial v'_k}{\partial x_k}}+\bar{\rho}R\widetilde{T'\frac{\partial v'_k}{\partial x_k}}\end{aligned} \tag{44}$$

is not yet closed. The temperature dilatation correlation $(\widetilde{T'\,\partial v'_k/\partial x_k})$ is extremely difficult to model and not much success has been achieved in dealing with it in the context of Reynolds stress models. However, within the framework of subgrid-scale modelling, this term and its corresponding cross-correlation have physical interpretations. They represent the contribution of the dilatation of the small scales to the internal energy variation of the fluid – an effect which is expected to be small. In fact, the recent direct numerical simulations of Sarkar *et al.* (1991) indicate that in compressible isotropic turbulence, the pressure–dilatation correlation – and therefore, the temperature dilatation – is extremely small. Hence, for this initial study, we neglect these terms. Furthermore, since the mean temperature is constant and the temperature fluctuations are small ($< 10\%$), the viscosity and thermal conductivity are held constant. For similar reasons, we also neglect the small-scale component of the viscous dissipation.

The turbulence model proposed herein is thus complete once values for the constants C_R and Pr_T are obtained. This will be accomplished using the results of direct numerical simulations of compressible isotropic turbulence.

3. Numerical method

Our direct simulations of compressible turbulence are based on a non-dimensional form of (1)–(3), with the time derivative in the energy equation written solely in terms of the pressure. In order to alleviate the severe stability limit imposed at very low Mach numbers by the acoustic waves, a splitting method is adopted. The first step integrates the equations

$$\frac{\partial \rho}{\partial t} = 0, \tag{45}$$

$$\frac{\partial(\rho v_k)}{\partial t} + \frac{\partial(\rho v_k v_l)}{\partial x_l} = \frac{\partial \sigma_{kl}}{\partial x_l}, \tag{46}$$

$$\frac{\partial p}{\partial t} + v_k \frac{\partial p}{\partial x_k} + \gamma p \frac{\partial v_k}{\partial x_k} - c_0^2 \frac{\partial(\rho v_k)}{\partial x_k} = \frac{1}{Re\,Pr\,M_0^2} \frac{\partial^2 T}{\partial x_k \partial x_k} + (\gamma - 1)\,\Phi, \tag{47}$$

while the second step integrates

$$\frac{\partial \rho}{\partial t} + \frac{\partial(\rho v_k)}{\partial x_k} = 0, \tag{48}$$

$$\frac{\partial(\rho v_k)}{\partial t} + \frac{\partial p}{\partial x_k} = 0, \tag{49}$$

$$\frac{\partial p}{\partial t} + c_0^2 \frac{\partial(\rho v_k)}{\partial x_k} = 0. \tag{50}$$

The constants c_0 and M_0 are the current root-mean-square (r.m.s.) value of the sound speed (c) and the reference Mach number, while $\gamma = C_p/C_v$, where C_v is the specific heat at constant volume. These equations are non-dimensionalized in terms of a lengthscale (L_0), a velocity scale (U_0), a pressure scale (P_0), a reference viscosity μ and a reference thermal conductivity κ. The Reynolds number is given by $Re = \rho_0 U_0 L_0/\mu$, the Prandtl number by $Pr = C_p \mu/\kappa$, and the reference Mach number by $M_0 = U_0/(\gamma R T_0)^{\frac{1}{2}}$. For all calculations presented in this study, $\gamma = 1.4$, and $Pr = 0.7$. Initially, the density ρ_0 is uniform and equal to one. The computational domain is a cube, normalized to $[0, 2\pi]^3$. Periodic boundary conditions are imposed in all three directions.

The spatial derivatives in these equations are approximated by a Fourier collocation method (see, for example, Hussaini & Zang 1987). In each coordinate direction, N grid points are used: $x_{k_j} = 2\pi j/N$, for $j = 0, 1, \dots, N-1$. The derivative of a function $\mathscr{F}(\boldsymbol{x})$ with respect to x_k is approximated by the analytic derivative of the trigonometric interpolant of $\mathscr{F}(\boldsymbol{x})$ in the direction x_k. Most simulations of incompressible, homogeneous turbulence have used a Fourier–Galerkin method. The compressible equations, however, contain cubic rather than quadratic nonlinearities and true Galerkin methods are more expensive (compared with collocation methods) than they are for incompressible flow. The essential difference between collocation and Galerkin methods is that the former are subject to both truncation and aliasing errors, whereas the latter have only truncation errors. As discussed extensively by Canuto *et al.* (1988), the aliasing terms are not significant for a well-resolved flow. However, care is needed to pose a collocation method in a form which ensures numerical stability. For this reason, the second term in (46) is actually used in the equivalent form

$$\frac{1}{2}\left[\frac{\partial(\rho v_k v_l)}{\partial x_l} + \rho v_l \frac{\partial v_k}{\partial x_l} + v_k \frac{\partial(\rho v_l)}{\partial x_l}\right]. \tag{51}$$

As noted by Feiereisen, Reynolds & Ferziger (1981), when this form is employed together with a symmetric differencing method in space (for example Fourier collocation), then in addition to mass and momentum, energy is conserved for the ideal compressible equations (zero viscosity and thermal conductivity) in the absence of time differencing (and splitting) errors.

The second fractional step of the splitting, given by (48)–(50), contains most of the effects of the acoustic waves. This splitting is employed at each stage of a third-order Runge–Kutta method. In the simulations reported here, the second fractional step is integrated analytically. In Fourier space, (48)–(50) become

$$\frac{\partial \hat{\rho}}{\partial t} + \mathrm{i} k_l \hat{m}_l = 0, \tag{52}$$

$$\frac{\partial \hat{m}_l}{\partial t} + \mathrm{i} k_l \hat{p} = 0, \tag{53}$$

$$\frac{\partial \hat{p}}{\partial t} + \mathrm{i} c_0^2 k_l \hat{m}_l = 0, \tag{54}$$

where $m_l = \rho v_l$ and Fourier transformed quantities (which depend upon the wavenumber $\boldsymbol{k}$) are denoted by a circumflex. The exact solution of these equations is

$$\hat{\rho}^{(2)} = \hat{\rho}^{(1)} + (1/c_0^2)\,[\hat{A}\cos(c_0 k \Delta t_s) + \hat{B}\sin(c_0 k \Delta t_s) - \hat{A}], \tag{55}$$

$$\hat{m}_l^{(2)} = \hat{m}_l^{(1)} - (\mathrm{i}k_l/c_0 k)\,[\hat{A}\sin(c_0 k \Delta t_s) - \hat{B}\cos(c_0 k \Delta t_s) + \hat{B}], \tag{56}$$

$$\hat{p}^{(2)} = \hat{A}\cos(c_0 k \Delta t_s) + \hat{B}\sin(c_0 k \Delta t_s), \tag{57}$$

where $k = |\boldsymbol{k}|$ is the magnitude of the Fourier wavenumber and

$$\hat{A} = \hat{p}^{(1)}, \quad \hat{B} = \mathrm{i}\,(c_0/k)\,k_l \hat{m}_l^{(1)}.$$

The superscript (1) denotes the result of the first fractional step of the splitting and the superscript (2) the results of the second fractional step. The effective time-step of the Runge–Kutta stage is denoted by Δt_s. The advantage of this splitting is that the principal terms responsible for the acoustic waves have been isolated. Since they are treated semi-implicitly, one expects the time-step limitation to depend upon the reciprocal of v rather than that of $v+c$. (Although there is also a viscous stability limit for the first fractional step, it is well below the advection limit in the cases of interest.) This is clearly a substantial advantage at low Mach numbers which has permitted us to use time-steps several times larger than those of the unsplit scheme. If one is truly interested in all the details arising from the sound waves, or if there is a substantial coupling between the sound waves and the rest of the flow, then the time-step must be small enough to resolve the temporal evolution of these waves. But, if only the larger-scale sound waves are of interest, then this splitting method is useful.

Some variations of this time splitting scheme have been shown by Abarbanel, Dutt & Gottlieb (1989) to be weakly unstable in the inviscid limit. However, the present scheme has been subjected to exhaustive tests in viscous flows where it was found to be stable and computationally robust.

During the acoustic fractional step, an isotropic truncation is performed: for each variable ($\rho, \rho v$ and p), all Fourier coefficients for which

$$k_l k_l \geqslant (\tfrac{1}{2}N)^2 \tag{58}$$

are set to zero. This reduces the numerical anisotropy produced by a cubic truncation. Moreover, it reduces the aliasing interactions in the collocation method (Canuto *et al.* 1988, Chapters 3 and 7).

The compressible code can also be executed in a purely explicit mode. In this case no splitting is performed; (45)–(50) are simply combined in the appropriate manner and integrated directly.

The expected stability limit of this three-dimensional Fourier collocation method for the compressible Navier–Stokes equations has the form

$$\Delta t < \alpha \left[\max_{\text{grid}} \sum_{i=1}^{3} \mathscr{U}_i \right]^{-1} \left(\frac{2\pi}{N} \right), \tag{59}$$

where

$$\mathscr{U}_i = |v_i| + |c| \tag{60}$$

when the time advancement is fully explicit. For the third-order Runge-Kutta method employed here, we use $\alpha = 0.5$. In the semi-implicit method, $\alpha \approx 1.5$.

A number of simulations of strictly incompressible flow have also been conducted. These were performed with a separate code which also used a Fourier collocation method, but for the simpler, incompressible Navier–Stokes equations.

4. Comparison with incompressible results

The initial conditions for the numerical simulations were designed to reproduce the experimental data of Comte-Bellot & Corrsin (1971) on isotropic turbulence, hereafter referred to as CBC. These experiments were also the basis of direct simulations used by Clark, Ferziger & Reynolds (1979), Bardina, *et al.* (1983), and McMillan & Ferziger (1979) in their analyses of incompressible large-eddy simulation(LES) models. Initial conditions are chosen to match CBC's measurements at a non-dimensional time of 240 (cf. table 4 in CBC). With the chosen non-dimensionalization, the Reynolds number $Re = U_0 L_0/\nu$ is 22.74 based on a kinematic

	CBC	64^3	96^3	128^3
v_{rms}	6.75	6.75	6.75	6.75
$\frac{1}{3}\mathrm{tr}(\boldsymbol{Sk})$	—	0	0	0
E	—	68.3	68.3	68.3
ϵ	462	375	432	447
λ_{11}	0.26	0.28	0.27	0.25
λ_{12}	—	0.20	0.19	0.27
λ_{13}	—	0.20	0.19	0.26
R_λ	38.1	43.4	40.5	39.8

TABLE 1. Initial conditions based on CBC experiment and Clark *et al.* (1979) calculation. Mach number is zero.

viscosity $\nu = 0.14\ \mathrm{cm}^2/\mathrm{s}$. Table 1 summarizes the parameters measured by CBC at $t = 240$. The Taylor microscale length λ_{kl} is defined by

$$\lambda_{kl} = \left[\frac{\langle v_k^2 \rangle}{\left\langle \left(\frac{\partial v_k}{\partial x_l}\right)^2 \right\rangle}\right]^{\frac{1}{2}} \tag{61}$$

and the total turbulent kinetic energy E and the dissipation ϵ by

$$E = \frac{1}{2}\int v_i v_i \,\mathrm{d}^3x, \qquad \epsilon = 2\mu \int S_{ij} S_{ij} \,\mathrm{d}^3x, \tag{62}$$

where S_{ij} is the rate of strain tensor

$$S_{ij} = \frac{1}{2}\left(\frac{\partial v_i}{\partial x_j} + \frac{\partial v_j}{\partial x_i}\right). \tag{63}$$

In (61), $\langle \cdot \rangle$ denotes a spatial average. Its exact definition is given in the Appendix. The Taylor microscale Reynolds number is

$$R_\lambda = \frac{v_1 \lambda_{11}}{\nu} = \left(\frac{20}{3}\right)^{\frac{1}{2}} R_t^{\frac{1}{2}}, \tag{64}$$

where $R_t \equiv E^2/(\nu\epsilon)$ is the turbulence Reynolds number. The velocity derivative skewness and flatness tensors $\boldsymbol{Sk}$ and $\boldsymbol{Fl}$ are the third and fourth moments of the velocity gradient and are defined by

$$Sk_{ij} = \left\langle \left(\frac{\partial v_i}{\partial x_j}\right)^3 \right\rangle \Big/ \left\langle \left(\frac{\partial v_i}{\partial x_j}\right)^2 \right\rangle^{\frac{3}{2}}, \tag{65}$$

$$Fl_{ij} = \left\langle \left(\frac{\partial v_i}{\partial x_j}\right)^4 \right\rangle \Big/ \left\langle \left(\frac{\partial v_i}{\partial x_j}\right)^2 \right\rangle^{2}. \tag{66}$$

In tables 1 and 2, only the traces of the skewness tensors are shown. The remaining columns list the parameters obtained from the initial conditions of the numerical simulations on 64^3, 96^3 and 128^3 grids. At the initial time, there is a nearly 20% discrepancy between the dissipation obtained by CBC and the dissipation computed on the coarsest grid, which suggests that a 64^3 grid has marginal resolution, at best.

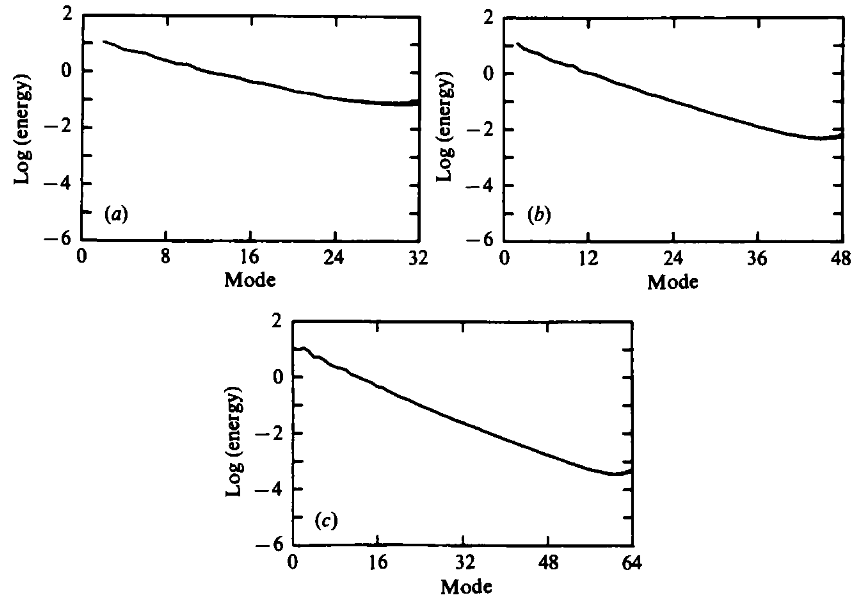

FIGURE 1. Energy spectra at $t = 0.0586$ for both aliased (— — —) and de-aliased (—) calculations for (*a*) 64^3, (*b*) 96^3, and (*c*) 128^3 grids.

	CBC	64^3	96^3	128^3
v_{rms}	5.03	5.18	5.19	5.21
$\frac{1}{3}\mathrm{tr}(\boldsymbol{Sk})$	—	−0.42	−0.51	−0.52
E	38.6	40.4	40.4	40.7
ϵ	154.4	152.0	154.6	156.8
λ_{11}	0.34	0.33	0.34	0.33
λ_{12}	—	0.24	0.24	0.23
λ_{13}	—	0.24	0.24	0.23
R_{λ}	36.6	39.5	40.0	39.8

TABLE 2. Final conditions ($t = 0.1145$) based on CBC experiment and Clark *et al.* (1979) calculation. Mach number is zero.

A 14% difference between the value of R_{λ} calculated on the 64^3 grid and that obtained by CBC confirms the need for grids finer than 64^3. On a 96^3 grid, both the dissipation and R_{λ} are in much closer agreement with CBC. Discrepancies between our results and CBC for ϵ and R_{λ} are respectively 6.5% and 6.3% on a 96^3 grid. On the finest grids on which the direct simulations were performed, the computed values of ϵ and R_{λ} respectively have relative errors of 3.2% and 4.5% when compared to CBC.

The numerical simulations were run from $t = 240$ until $t = 375$ (in CBC units), which corresponds to a non-dimensional time interval of 0.1145 (in our units). Table 2 furnishes a comparison of the experimentally measured parameters with those from the numerical simulation at the final time. On the coarsest grid, the total dissipation rate that was calculated is still slightly below the value measured by CBC. A 96^3 grid generates values of ϵ consistent with CBC.

At $t = 0.1145$, the diagonal components of $\boldsymbol{Sk}$ are -0.5 which agree well with the numerical results of Kerr (1985). Kerr studied isotropic, turbulent flow, but prevented the decay of energy by using an exterior energy source at the large lengthscales.

As noted in the previous section, we have chosen not to de-alias the advection terms. In reaching this decision we drew upon the extensive evidence that has accumulated on aliasing effects in the last dozen years (Canuto *et al.* 1988, Chapters 3, 4 and 7) and upon tests conducted with the incompressible isotropic turbulence code. In this code, de-aliasing is accomplished by applying the $\frac{2}{3}$-rule (Canuto *et al.* 1988, Chapters 3 and 7) in an isotropic fashion; e.g. the de-aliased results for a 64^3 grid are obtained by running the incompressible code on a 96^3 grid and applying the truncation given by (58) with $\frac{1}{3}N$ in place of $\frac{1}{2}N$ on the right-hand side. The results are summarized in figure 1. Here we present the energy spectra $E(k)$ (defined in the Appendix) for 64^3, 96^3, and 128^3 grids at $t = 0.0586$ for both aliased and de-aliased calculations. Some adverse effects of aliasing are apparent on the 64^3 grid, but they are only in the tail of the spectra, and they are already insignificant on a 96^3 grid. For the reasons outlined here, a 96^3 grid was chosen as the standard discretization for the incompressible and for the compressible simulations.

5. Compressible turbulence results

5.1. *Direct simulations*

Recent work on the direct numerical simulation of homogeneous compressible turbulence has indicated the crucial role played by the initial conditions. Passot & Pouquet (1987) conducted direct simulations of two-dimensional, compressible isotropic turbulence and concluded that when the initial r.m.s. density fluctuations are small, the turbulence statistics remain quasi-incompressible for turbulent Mach numbers M_t less than 0.3, where

$$M_t = M_0 \left\langle \frac{v^2}{T} \right\rangle^{\frac{1}{2}}. \tag{67}$$

They also demonstrated (through the use of direct numerical simulations) that eddy shocklets result for sufficiently high initial r.m.s. density fluctuations and/or turbulent Mach numbers. A more systematic analysis and categorization of the effect of the initial conditions on compressible isotropic turbulence was achieved recently by Erlebacher *et al.* (1990) (see also Blaisdell, Mansour & Reynolds 1991 and Sarkar *et al.* 1991).

Passot & Pouquet (1987) concluded that for $0 < M_t < 0.3$, p_{rms} must initially be $O(M_t)$ for the resulting turbulence statistics to become strongly compressible with an $O(1)$ ratio of compressible to incompressible turbulent kinetic energy. (For the range of M_t considered herein, no eddy-shocklets occur.) On the other hand, if ρ_{rms}, $T_{\mathrm{rms}} \ll M_t$ initially, then the resulting turbulence statistics remain quasi-incompressible. Unless specified otherwise, a subscript rms for any variable $\mathscr{F}$ refers to the quantity $\langle(\mathscr{F}-\langle\mathscr{F}\rangle)^2\rangle^{\frac{1}{2}}/\langle\mathscr{F}\rangle$.

We first present the results of direct numerical simulations of compressible isotropic turbulence corresponding to the initial conditions of the CBC experiment but with a variety of non-zero mean Mach numbers. Since the initial conditions for these simulations are $\rho_{\mathrm{rms}} = 0$, $T_{\mathrm{rms}} \ll 1$, only weakly compressible turbulence statistics are expected according to the theoretical results of Erlebacher *et al.* (1990). The initial pressure distribution over the entire field is specified. The fluctuating pressure, p_f is determined from the velocity distribution by enforcing a zero initial

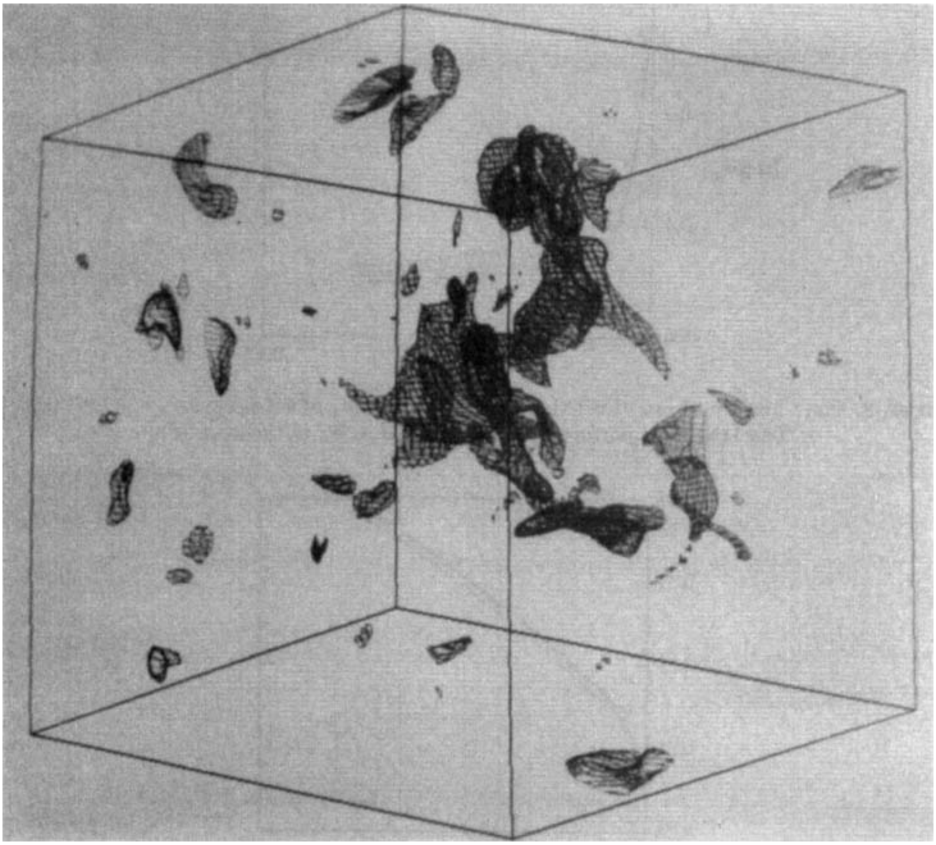

FIGURE 2. Three-dimensional Mach 1.0 contour levels of the DNS data at $t = 0.0586$, performed on a 96^3 grid.

time derivative for $\nabla \cdot v$. A Poisson equation for p_f is obtained from the divergence of the momentum equation after setting the time variation of $\nabla \cdot v$ to zero (Feiereisen *et al.* 1981). The mean pressure, p_m, is then determined so that a prescribed initial mean average Mach number, M_0, defined to be the ratio of r.m.s. fluid velocity and r.m.s. speed of sound, is achieved. An analytic expression for p_m is given by

$$\langle p_m \rangle = \frac{\langle v^2 \rangle}{\gamma M_0^2} - \langle p_f \rangle. \tag{68}$$

The initial average Mach number is specified at the outset of the direct numerical simulations (DNS) as an initial condition. Density is initially set to unity, while the temperature, if required, is derived from the equation of state. Direct numerical simulations are performed for $M_0 = 0$, 0.1, 0.4 and 0.6. For these initial conditions, quasi-incompressible turbulence statistics result. Initial conditions that are more in line with those of Passot & Pouquet (1987) – which give rise to significant compressible turbulence statistics – are used later for the large-eddy simulations.

The Mach 0.6 case contains localized regions of supersonic flow as evidenced by tables 3 and 4 and by the three-dimensional Mach 1 contour level furnished in figure 2. Nonetheless, the statistical properties of the flow remain largely unaffected by compressibility. This is shown in figures 3–6 which track the time histories of several

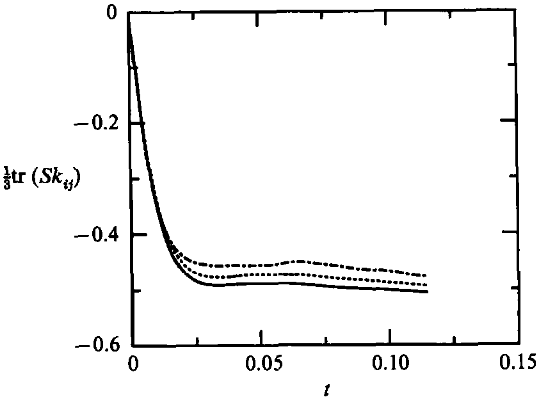

FIGURE 3. Time history of one third the trace of **Sk** for M_0 of 0.1 (—), 0.4 (----) and 0.6 (–·–·–). The DNS was performed on a 96^3 grid. CBC initial conditions.

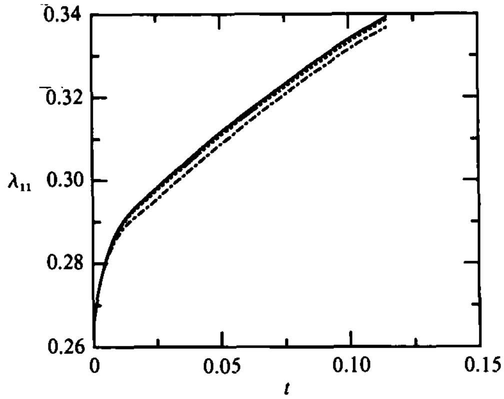

FIGURE 4. Time history of Taylor microscale for M_0 of 0.1 (—), 0.4 (----) and 0.6 (–·–·–). The DNS was performed on a 96^3 grid. CBC initial conditions.

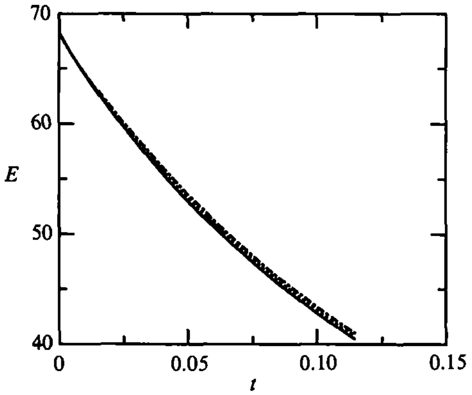

FIGURE 5. Time history of kinetic energy for M_0 of 0.1 (—), 0.4 (----) and 0.6 (–·–·–). The DNS performed on a 96^3 grid. CBC initial conditions.

statistical variables obtained from 96^3 DNS. The time histories for skewness (figure 3), λ_{11} (figure 4), and total kinetic energy (figure 5) at Mach numbers 0.1, 0.4 and 0.6 are, for the most part, superimposed on each other.

Flatness and skewness are affected by compressibility the most in these

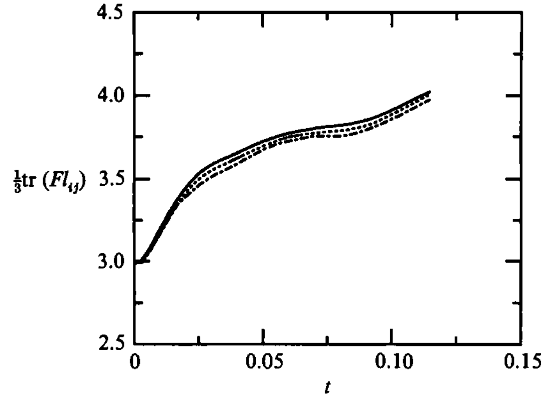

FIGURE 6. Time history of one third the trace of ***Fl*** for M_0 of 0.1 (—), 0.4 (– – – –) and 0.6 (– - – -). The DNS was performed on a 96^3 grid. CBC initial conditions.

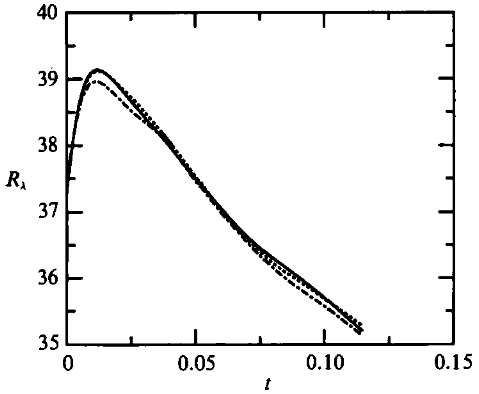

FIGURE 7. Time history of R_λ for M_0 of 0.1 (—) 0.4 (----) and 0.6 (– - – -). The DNS was performed on a 96^3 grid. CBC initial conditions.

simulations. Figure 3 indicates that the skewness which corresponds to an isotropic turbulent state monotonically increases with Mach number. It is -0.50 at $M_0 = 0$ and has increased to -0.46 at $M_0 = 0.6$. Before the flow has reached a state of isotropic turbulence, the time evolutions of skewness at all Mach numbers are indistinguishable from each other. The physical system has equilibrated after approximately one third the total computation time. While not reaching an equilibrium value, it is nonetheless worthwhile to point out that the flatness parameter decreases by 2 % as the Mach number is raised from 0 to 0.6 as seen in figure 6.

Figure 5 illustrates the decay of turbulent kinetic energy (E) as a function of time. This decay is a natural consequence of viscous damping. After a brief initial increase, R_λ continuously decreases in time (figure 7) with no sign of stabilizing. On the other hand, λ which is representative of the smaller eddies, increases in time (figure 4). This indicates that energy in the higher wavenumbers is being depleted by the molecular viscosity.

Tables 3–5 summarize the results of direct simulations of compressible isotropic turbulence for $M_0 = 0.1$, 0.4 and 0.6, for $t = 0.1145$ on three different grids. (A DNS at $M_0 = 0.6$ was not performed on the 128^3 grid.) Incompressible results are included

M_0	E	ϵ	$\lvert\nabla\cdot\boldsymbol{v}\rvert_{\max}$	$\langle\frac{1}{3}\mathrm{tr}(\boldsymbol{Sk})\rangle$	$\langle M_t\rangle$	$(M_t)_{\max}$
0	40.26	157.4	0	−0.424	0	0
0.1	40.82	158.2	0.17	−0.440	0.07	0.21
0.4	41.09	160.4	1.50	−0.428	0.28	0.84
0.6	41.32	162.3	3.30	−0.406	0.43	1.26

TABLE 3. Summary of direct simulations on a 64^3 grid with initial average Mach numbers of 0, 0.1, 0.4 and 0.6 at $t = 0.1145$

M_0	E	ϵ	$\lvert\nabla\cdot\boldsymbol{v}\rvert_{\max}$	$\langle\frac{1}{3}\mathrm{tr}(\boldsymbol{Sk})\rangle$	$\langle M_t\rangle$	$(M_t)_{\max}$
0	40.35	154.3	0	−0.506	0	0
0.1	40.49	155.5	0.14	−0.505	0.07	0.23
0.4	40.79	157.0	1.17	−0.493	0.28	0.93
0.6	41.04	158.3	2.82	−0.477	0.42	1.39

TABLE 4. Summary of direct simulations on a 96^3 grid with initial average Mach numbers of 0, 0.1, 0.4 and 0.6 at $t = 0.1145$

M_0	E	ϵ	$\lvert\nabla\cdot\boldsymbol{v}\rvert_{\max}$	$\langle\frac{1}{3}\mathrm{tr}(\boldsymbol{Sk})\rangle$	$\langle M_t\rangle$	$(M_t)_{\max}$
0	40.73	156.81	0	−0.521	0	0
0.1	40.39	154.84	0.14	−0.518	0.07	0.21
0.4	40.78	156.54	1.11	−0.505	0.28	0.86

TABLE 5. Summary of direct simulations on a 128^3 grid with initial average Mach numbers of 0, 0.1 and 0.4 at $t = 0.1145$

for comparison. On all the grids, the compressible data converge to the incompressible results as the Mach number is driven towards zero. As expected, the divergence of velocity no longer vanishes, and is now an increasing function of M_0.

While the dissipation is approximately the same on the two finer grids, the consistently lower values on the coarsest grid confirm the previously stated conclusion that a 64^3 grid cannot resolve all the lengthscales. As a function of increasing Mach number, the trace of $\boldsymbol{Sk}$ increases while the trace of $\boldsymbol{Fl}$ decreases.

The results in tables 3–5 are averages over several DNS runs with different initial seeds. A given seed uniquely determines the initial velocity distribution, and therefore the pressure and temperature fields. Variations of the seed are only necessary to eliminate the statistical uncertainty due to the random velocity distribution. The distributions of velocity on two different grid sizes are different even when the initial seed is the same.

Skewness is even more sensitive to the grid refinement than the dissipation as witnessed by its decrease from -0.506 to -0.521 on 96^3 and 128^3 grids, respectively, for $M_0 = 0$. This might be a result of the greater sensitivity of the fluctuating velocity field spatial derivatives to slight inaccuracies in the flow variables.

5.2. *Data analysis*

Using the data generated from the previously discussed DNS of compressible homogeneous turbulence on a 96^3 grid at low Mach numbers, the proposed subgrid-scale model is now validated. Models relate the subgrid-scale stresses – which are not available to a large-eddy simulation code – to the large-scale velocities, which are known. These velocities are simply the Favre-filtered velocities introduced earlier.

The Favre-filtered velocities are calculated by filtering the resolved DNS velocity field with a Gaussian spatial filter of width $\Delta = \Delta_f \Delta x_f$, where Δx_f is the grid spacing on the fine grid. For convenience, Δ_c and Δ_f refer to the filter width Δ non-dimensionalized with respect to the coarse and fine grid spacing respectively.

Perturbed velocity fluctuations on the fine grid are the difference between the fully resolved velocity and the filtered ones, given by

$$\boldsymbol{v}' = \boldsymbol{v} - \tilde{\boldsymbol{v}}. \tag{69}$$

From $\boldsymbol{v}'$ and $\tilde{\boldsymbol{v}}$, subgrid-scale stresses based on DNS, referred to as exact, are calculated. These include the Leonard, cross- and Reynolds subgrid-scale stresses given by (20)–(22). However, these subgrid-scale stresses themselves do not directly affect the evolution of the system. The momentum equation is only influenced by the divergence of the subgrid-scale stresses (i.e. the vector level). Similarly, $\tilde{\boldsymbol{v}} \cdot (\boldsymbol{\nabla} \cdot \boldsymbol{\tau})$ (the scalar level) is a better representation of the dissipation terms in the energy equation than are the stresses. Consequently, correlations are performed on the tensor, vector and scalar levels. Ideally, high correlations are desired on all levels.

The data analysis proceeds in multiple stages. First, the exact stresses calculated from the DNS are injected down to the coarse grid, along with the filtered velocities. The modelled subgrid-scale stresses are then calculated (excluding the model constants) on the coarse grid. Some variables must be filtered a second time (e.g. cross-stress terms). Rather than calculate them on the fine grid (which is not available to the large-eddy simulation codes), a Gaussian filter is applied to $\tilde{\boldsymbol{v}}$ on the coarse grid with a filter width of Δ_c. Consistency between the coarse and fine filter widths is achieved by ensuring that

$$\frac{\Delta_f}{\Delta_c} = \frac{N_f}{N_c}, \tag{70}$$

where N_f and N_c are respectively the number of nodes along one direction of the fine and coarse grids. This guarantees that the filtering on the coarse and fine grids is performed over the same region in physical space. Derivative evaluations on both the coarse and the fine grid are based on Fourier collocation. Calculations by McMillan & Ferziger (1979) indicate that the model constants are sensitive to the accuracy of the derivative evaluations. A general trend that has been observed is that the Smagorinsky constant is lowered when derivative quantities are evaluated more accurately. Our constants are therefore expected to lie in the lower range of the values obtained by McMillan (1980).

Next, the model constant, C_R, is calculated. Unfortunately, the constants can be calculated by a wide variety of algorithms, each with its own merits. Moreover, for each algorithm, the constants can be evaluated from tensor, vector or scalar information. Therefore, criteria must be established to identify the best method. A key test is that $\boldsymbol{L} + \boldsymbol{C}$ should be Galilean invariant. To make use of this fact, an additional constant, C_C, is introduced as an extra factor in the subgrid-scale cross-stress model. A self-consistent method of calculating the constants must reproduce $C_C = 1$ to satisfy the Galilean invariance property stated above (Speziale 1985). Additional tests are performed on coarse grids with varying degrees of refinement which further decrease the number of choices. A thorough discussion of model constants is the subject of the next subsection.

Once a single or a multiple set of model constants has been determined, the model subgrid-scale stresses are calculated and correlated with the exact subgrid-scale stresses calculated from the DNS after injection onto the coarse grid. The correlations are performed for each type of subgrid-scale stress individually, and for the total stress ($\boldsymbol{L}+\boldsymbol{C}+\boldsymbol{R}$). Strong differences in the correlation coefficients relating total stresses are noticed depending on whether or not the Leonard stresses are included. Finally, the correlations obtained from the proposed model are compared with the linear combination model, which has been shown to be one of the best models available for incompressible isotropic turbulence. Correlation coefficients are calculated based on the two pairs of constants that are obtained from the above considerations. The set that is finally retained corresponds to the highest levels of correlation of the total stress on the vector and scalar levels. These matters are treated more completely in a later subsection.

5.2.1. *Model constants*

The proposed model given by (31) and (42) has two undetermined coefficients. The constant, C_R, is associated with the modelled subgrid-scale Reynolds stress, $\boldsymbol{R}$, while Pr_T is associated with the Reynolds heat flux.

Although the cross-stress model has no constant associated with it, it is nonetheless multiplied by a constant C_C. This is done in the hope of reducing the number of schemes by which the constants can be calculated. A good model should reproduce a cross-stress constant of one to guarantee Galilean invariance. Once the constants have been determined, C_C is set to one and forgotten. Because the flow is isotropic, constants are expected to be the same for the three diagonal stress components, the three off-diagonal components and the three vector components. Therefore, the values presented in the tables below are averaged over the appropriate components. In the tables, D refers to averaged diagonal components, OD to averaged off-diagonal components, V to averaged vector components and S to averaged scalar components. Similar averagings are performed for the correlation coefficients.

The two constants (C_R and C_C) are calculated using two techniques – each applied on the tensor, vector and scalar levels (see the Appendix for further details). One method enforces equality of the r.m.s. levels of the exact and modelled stresses. This is done for each individual subgrid-scale stress (i.e. the subgrid-scale Reynolds stress and the cross-stress). Hereafter this approach is referred to as RMS. The second method utilizes multiple linear least-square regression (LSQ) between the exact (18) and the modelled (31) total subgrid-scale stresses to determine the constants. Table 6 summarizes the results obtained from incompressible data. The three cases presented are identical except for the initial random number seed. The constants are independent of the detailed velocity statistics. These results are based on a vector level comparison between the modelled and exact stresses. Both RMS and LSQ produce C_C close to unity as required. Unfortunately this prevents a rational choice from being made between the two approaches. A more complete set of LSQ constants is presented in table 7. They are computed at Mach numbers of 0, 0.1, 0.4 and 0.6 on the tensor, vector and scalar level. Computations are performed on a coarse grid of 16^3.

At first glance, C_C is near unity at both the scalar and vector levels. However, whereas on the vector level the constant remains within 4% of unity for all Mach numbers, this is not the case on the scalar level where C_C is a decreasing function of Mach number. This trend is present in the data generated from both random seeds. Although not presented here, the r.m.s. cross-stress model constant is also near unity when calculated based on vector level stresses. Therefore, a preferred method for the determination of the model constants is still not possible.

	LSQ		RMS	
Seed	C_R	C_C	C_R	C_C
1	0.012	1.04	0.023	1.03
2	0.012	1.03	0.022	1.04
3	0.012	1.03	0.022	1.03

TABLE 6. Model constants calculated by LSQ and RMS between exact and modelled total stresses $(\boldsymbol{L}+\boldsymbol{C}+\boldsymbol{R})$. Results are based on three identical incompressible simulations except for the random initial velocity distributions. Calculations are on the vector level on a 16^3 grid.

		Seed 1				Seed 2	
M_0		0	0.1	0.4	0.6	0	0.6
	D	1.32	1.32	1.32	1.31	1.32	1.31
C_C	V	1.04	1.04	1.02	1.00	1.04	1.00
	S	1.00	1.00	0.95	0.873	0.971	0.934
	D	0.018	0.018	0.018	0.018	0.016	0.015
C_R	V	0.012	0.012	0.012	0.012	0.012	0.012
	S	0.015	0.015	0.015	0.014	0.015	0.015

TABLE 7. LSQ model constants. Filter widths are $\Delta_f = 12$ and $\Delta_c = 2$.

	LSQ			RMS		
Δ_f	6	12	24	6	12	24
Δ_c	1	2	4	1	2	4
C_R	0.007	0.012	0.020	0.019	0.023	0.034
C_C	0.31	1.03	1.33	0.82	1.03	1.13

TABLE 8. LSQ and RMS model coefficients between exact and modelled stresses on the vector level at $M_0 = 0.1$. Results are obtained with fine filter widths of 6, 12 and 24 while maintaining the proper ratio of 6 between fine and coarse widths. The coarse grid is 16^3.

5.2.2 *Filter width and grid coarseness*

Confirmation of the numerical evidence presented by McMillan & Ferziger (1979) that $\Delta_c = 2$ is the best filter width is given in table 8 ($M_0 = 0.1$). The criterion used to determine the validity of the filter width is that C_C^{RMS} must remain close to unity on the vector level. Only when $\Delta_c = 2$ is C_C near one. Similar results hold for LSQ constants. The constants also vary with respect to the coarse grid on which the LES is to be performed. Table 9 summarizes the model LSQ and RMS constants evaluated from modelled stresses calculated on 16^3 and 32^3 grids on the vector level. The data ($M_0 = 0.1$) show that C_R varies by 30% when the grid size on which the modelled stresses are calculated changes from 16^3 to 32^3. On the other hand, large-eddy simulations using finite-difference algorithms might be performed on grids as large as 128^3. Unless a subgrid-scale model is found which produces constants independent of the coarse grid size, LES will run the risk of producing the wrong results. Perhaps a more complicated dependence of the modelled subgrid-scale Reynolds stresses on Δ is required.

The best model constants will produce the highest correlations between the modelled and exact subgrid-scale stresses on all levels (tensor, vector and scalar).

	LSQ		RMS	
Grid	C_R	C_C	C_R	C_C
16^3	0.0125	1.03	0.023	1.03
32^3	0.0094	1.03	0.013	1.02

TABLE 9. LSQ and RMS model constants based on subgrid-scale stresses evaluated on 16^3 and 32^3 coarse grids

Based on the previous discussion, only constants calculated on a vector level are adequate because they produce a C_C of unity. Unfortunately, a clear cut choice between RMS and LSQ constants cannot be made because C_C (on the vector level) is nearly one in both cases. Rather than make an arbitrary choice, both sets of constants are considered when correlating exact against modelled stresses. For reference, the constants used henceforth are

$$C_R^{\mathrm{LSQ}} = 0.012, \tag{71}$$

$$C_R^{\mathrm{RMS}} = 0.023. \tag{72}$$

5.2.3. *Correlations*

Correlation coefficients have long been a preferred diagnostic tool for estimating the reliability of the modelled stresses. However, the subgrid-scale stresses have been separated into various components ($\boldsymbol{L}, \boldsymbol{C}, \boldsymbol{R}$), each modelled separately and although the correlation of any of these components against their models might be excellent, it is still possible for the correlation of the exact total stress against the modelled total stress to be less impressive. Such is the case, for instance, when two stress components have opposite signs and partially cancel each other out. As a final note, before the specific correlation coefficients are presented, one must always be attentive to the actual relationship between the exact and the modelled variable, even when the correlation coefficient is relatively high (say, above 70%). A correlation coefficient as high as 70% may not be as good as it seems. For example, the correlation between the functions $y = x$ and $y = \exp(-x)$ in the interval $[0, 1]$ is approximately 70% although they are qualitatively different functions! As a consequence, correlations are only deemed good if the correlation coefficient is above, say, the 90% level.

For convenience, the compressible subgrid-scale model is restated here:

$$_{\mathrm{D}}R_{ij} = 2C_R \bar{\rho}\Delta^2(\tilde{S}_{kl}\tilde{S}_{kl})^{\frac{1}{2}}(\tilde{S}_{ij} - \tfrac{1}{3}\tilde{S}_{mm}\delta_{ij}), \tag{73}$$

$$_{\mathrm{I}}R_{ij} = 0, \tag{74}$$

$$C_{ij} = -\bar{\rho}(\tilde{v}_i\tilde{v}_j - \tilde{\tilde{v}}_i\tilde{\tilde{v}}_j). \tag{75}$$

The correlation coefficients presented in table 10 between exact and modelled $\boldsymbol{R}$ and $\boldsymbol{C}$ are independent of the model constants. The correlation coefficients are insensitive to the average Mach number variation. The neglect of $_{\mathrm{I}}R_{ij}$ appears to be a good approximation; the direct simulations show it to be several orders of magnitude smaller than the thermodynamic pressure. For example, for all of the compressible isotropic turbulence simulations conducted in this study,

$$\frac{(\nabla \cdot {}_{\mathrm{I}}\boldsymbol{R})_{\mathrm{rms}}}{(\nabla p)_{\mathrm{rms}}} < 3 \times 10^{-3} \tag{76}$$

M_0		0.1	0.4	0.6
	D	31	31	31
$\boldsymbol{R}$	OD	26	26	25
	V	22	22	22
	S	45	45	45
	D	89	89	89
$\boldsymbol{C}$	OD	91	91	91
	V	80	80	80
	S	75	74	72

TABLE 10. Correlations between exact and modelled stresses, $\boldsymbol{R}$ and $\boldsymbol{C}$, at Mach 0.1, 0.4 and 0.6

	$M_0 = 0$		$M_0 = 0.6$	
	$\boldsymbol{L}+\boldsymbol{C}+\boldsymbol{R}$	$\boldsymbol{C}+\boldsymbol{R}$	$\boldsymbol{L}+\boldsymbol{C}+\boldsymbol{R}$	$\boldsymbol{C}+\boldsymbol{R}$
D	93	82	93	81
OD	80	85	79	84
V	46	72	46	71
S	56	73	56	74

TABLE 11. Comparison of correlation coefficients of the exact total stress versus its model. The modelled terms are computed on a 16^3 coarse grid. Each case is presented with and without the inclusion of the Leonard subgrid-scale stress terms (calculated exactly). Both the incompressible and the $M_0 = 0.6$ case are shown to illustrate the weak influence of Mach number on the correlation coefficients with $C_R = 0.012$.

and, hence, the effect of the isotropic part of the Reynolds stress tensor is dominated by the thermodynamic pressure.

In most of the literature on subgrid-scale models, the Leonard stress has been omitted from the total stress correlations on the grounds that it is calculated exactly (Bardina *et al.* 1983; McMillan 1980; McMillan & Ferziger 1979). However, it has recently been shown by Speziale (1985) that the combination $\boldsymbol{L}+\boldsymbol{C}$ is Galilean invariant, while the Leonard and cross-stresses, individually, are not. Therefore we feel that correlations of the total stress should include the Leonard stress. Table 11 summarizes the correlation coefficients between the total stress including and excluding the Leonard stress. Results are presented at Mach 0 and 0.6. When the Leonard stresses are left out, correlation coefficients similar to those of Bardina *et al.* are obtained on all levels. However, the inclusion of $\boldsymbol{L}$ decreases the correlations at the vector level by approximately 30%. Table 11 substantiates that the correlation coefficients (with and without $\boldsymbol{L}$) are nearly independent of the initial average Mach number.

Correlation coefficients between $(\boldsymbol{C}+\boldsymbol{R})^e$ (where e denotes 'exact') and various combinations of the modelled stresses using constants calculated by LSQ and RMS are summarized in table 12. The second column indicates the model against which the total stress is being compared. Although at first glance RMS-based constants perform better at the tensor level when the total modelled stress is considered, at the vector and scalar levels, the trend is reversed. Correlations at the vector and scalar levels are higher by 4% using the LSQ constants.

When the constants are selected based on LSQ, table 12 indicates that the correlations on all levels are highest when all modelled components are included.

		LSQ				RMS			
		$C_R = 0.0122$				$C_R = 0.023$			
Exact	Model	D	OD	V	S	D	OD	V	S
$\boldsymbol{C}+\boldsymbol{R}$	$\boldsymbol{C}$	78	82	68	62	78	82	68	62
	$\boldsymbol{C}+\boldsymbol{R}$	81	84	71	70	88	83	67	67

TABLE 12. Correlation of the exact total stress $(\boldsymbol{C}+\boldsymbol{R})^e$ with various models. The modelled stresses are defined in equations (73)–(75).

However, the dynamic evolution of the large-scale velocities only brings into play the stresses on the vector and scalar level. Therefore the coefficients which produce the maximum correlations of total stress on these two levels should be chosen. This leads to an optimum choice of

$$C_R = 0.012, \tag{77}$$

calculated by least-squares fit of the total stress on the vector level.

Conversion of C_R to the standard form currently used in incompressible LES† produces a Smagorinsky constant of 0.092. McMillan (1979) obtained a value of $C_S = 0.10$ when spectral collocation derivative computations were employed. This constant corresponds to a scalar level evaluation based on LSQ. On the vector level, McMillan calculated a higher Smagorinsky constant of 0.13. This value can be obtained from the present data by using ${}_{\mathrm{D}}\boldsymbol{R}^{\mathrm{RMS}}$ instead of ${}_{\mathrm{D}}\boldsymbol{R}^{\mathrm{LSQ}}$. However, as shown above, the correlations of the total subgrid-scale stress would be lower.

Initial tests of the subgrid-scale heat flux model produced a turbulent Prandtl number in the range of 0.4 to 0.5. For this initial study, we take

$$Pr_{\mathrm{T}} = 0.5, \tag{78}$$

which is a value that has been used in previously published large-eddy simulations of turbulent flows with thermal convection (cf. Eidson 1985). A more accurate calculation of Pr_{T} could be accomplished in a compressible flow with significant mean temperature gradients; this is beyond the scope of the present study and must await future research.

6. Large-eddy simulation of compressible isotropic turbulence

In order to demonstrate the efficacy of the subgrid-scale models derived in this paper, a large-eddy simulation of compressible isotropic turbulence is now conducted. Since most high-speed compressible turbulent flows have significant regions where the turbulence statistics are quasi-incompressible, it is important that the models perform well for weakly compressible turbulence – the type of flow considered in the last section for the *a priori* tests. However, it is well known that *a priori* tests only provide a relatively weak gauge for the performance of subgrid-scale models in an actual large-eddy simulation (see Hussaini, Speziale & Zang 1990). It is therefore important to examine their performance in an actual large-eddy simulation, particularly for a case where significant compressibility effects are exhibited in the turbulence statistics.

---

† In a number of reports (McMillan & Ferziger 1979, Bardina *et al.* 1983), the subgrid-scale Reynolds stress model is proportional to C_S^2. In these cases, the relationship between C_S and C_R is $C_R = \sqrt{2}C_S^2$.

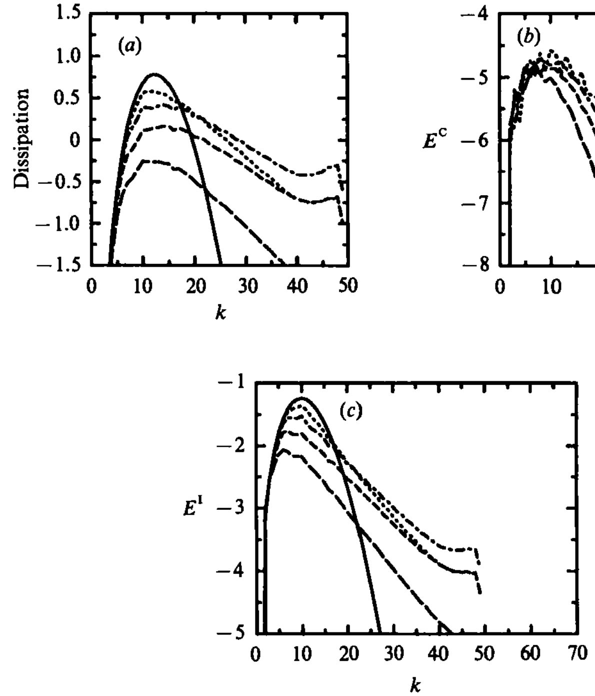

FIGURE 8. Log of energy and dissipation spectra of 96^3 DNS at $t = 0$ (—), 0.2 (----), 0.4 (– – –) 0.8 (– –), 1.6 (— —). $k_0 = 10$, $\chi_0 = 0$, $(M_t)_0 = 0.1$, $(R_\lambda)_0 = 30.0$, $Re = 250$. (*a*) Dissipation, (*b*) compressible energy, (*c*) solenoidal energy.

Direct simulations of compressible isotropic turbulence were conducted corresponding to the initial conditions $Re = 250$, $\langle M_t^2 \rangle_0^{\frac{1}{2}} = 0.1$, $\langle \rho \rangle_0 = 1$, $\langle T \rangle_0 = 1$, $(\rho_{\mathrm{rms}})_0 = 0$, $(T_{\mathrm{rms}})_0 = 0.0626$ and two values of χ_0: 0 and 0.2 which, respectively, correspond to initial values for $(R_\lambda)_0$ of 30.0 and 26.3. Here, $\chi = E^C/(E^I + E^C)$, where E^I and E^C are the incompressible and compressible parts of the turbulent kinetic energy, respectively. The direct numerical simulations were performed on a 96^3 mesh. Log plots of the characteristic energy and dissipation spectra associated with the DNS are shown in figures 8(*a*)–(*c*) and 9(*a*)–(*c*) for $\chi_0 = 0$ and 0.2, respectively. Figure 8(*b*) clearly shows that χ remains very small for all time, with only very slight modification of the energy spectrum over time. In contrast, figure 9(*b*) shows an initial cascade of the spectrum towards the smaller scales, followed by a strong energy dissipation at the smaller scales of v_i^C. The dissipation spectra $(k^2E(k))$ shown in figures 8(*a*) and 9(*a*) demonstrate that both the small and large scales are well resolved. Comparing figures 8(*c*) and 9(*c*), the shape of the energy spectra $E^I(k)$ are the same at $t = 0$, but are affected by compressibility at the later times. This influence is characterized by a slight decrease in $E^I(k)$ for $\chi_0 > 0$.

Integral properties of these two cases are plotted in figure 10(*a*)–(*f*). This figure contrasts the two runs corresponding to $\chi_0 = 0$ and 0.2. The higher compressibility has a variety of effects on the flow. The total kinetic energy decays at a slightly slower rate, while both the skewness and the flatness are decreased. In other words, finite compressibility drives the flow more towards a Gaussian state. Both the integral scale L_I and the Taylor microscale λ_{11} become smaller as χ_0 increases. Lastly, the decay rate of the microscale Reynolds number is slower for finite χ_0. A more detailed study of these effects awaits future research. It would be particularly useful

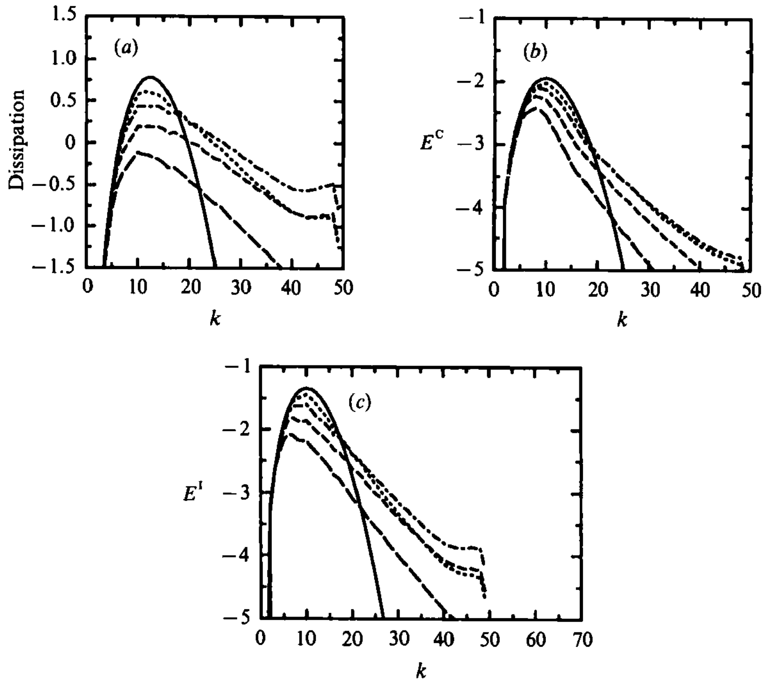

FIGURE 9. Same as figure 8 but for $\chi_0 = 0.2$, $(M_t)_0 = 0.1$, $(R_\lambda)_0 = 26.4$, $Re = 250$.

to compute these statistical quantities based on the solenoidal and irrotational components of velocity.

As noted by Frisch & Orszag (1990), the three-dimensional vorticity $\boldsymbol{\omega}$ is formed of tubular-like structures. This is graphically represented in figure 11 which shows a volume rendering of $\boldsymbol{\omega}^2$. Volumetric rendering is a visualization technique whereby rays are projected from the eye through the flow (which emits and absorbs light). The tubular structures of vorticity are contrasted with the spherical structure of $(\boldsymbol{\nabla} \cdot \boldsymbol{v})^2$ shown in figure 12. This difference is to be expected since the dilatation satisfies an isotropic wave equation to leading order which shows no preferential direction. On the other hand, the vorticity stretching occurs along the axis of the vorticity vector, which then becomes a preferred direction.

The results for the direct simulation with the strongest compressibility effects ($\chi_0 = 0.2$) were filtered and injected onto a coarse 32^3 grid for comparison with an LES which was also performed on a 32^3 grid using the subgrid-scale models derived herein. In this manner, a direct comparison can be made between the results of the LES and the direct simulation for a flow where the turbulence statistics exhibit significant compressibility. The following turbulence statistics were compared:

(i) the integrated average of $\omega_i \omega_i$ and $(\partial v_i/\partial x_i)^2$;

(ii) the integrated average total and isotropic vortex stretching ($\omega_i S_{ij} \omega_j$ and $\omega^2 \boldsymbol{\nabla} \cdot \boldsymbol{v}$, respectively);

(iii) the mean turbulence Mach number $\langle M_t^2 \rangle^{\frac{1}{2}}$;

(iv) the mean compressible, incompressible and total turbulent kinetic energy E^C, E^I and E, respectively;

(v) the level of compressibility $\chi = E^C/E$; and

(vi) the r.m.s. of the thermodynamic pressure, density, and temperature; p_{rms}, ρ_{rms}, and T_{rms}, respectively.

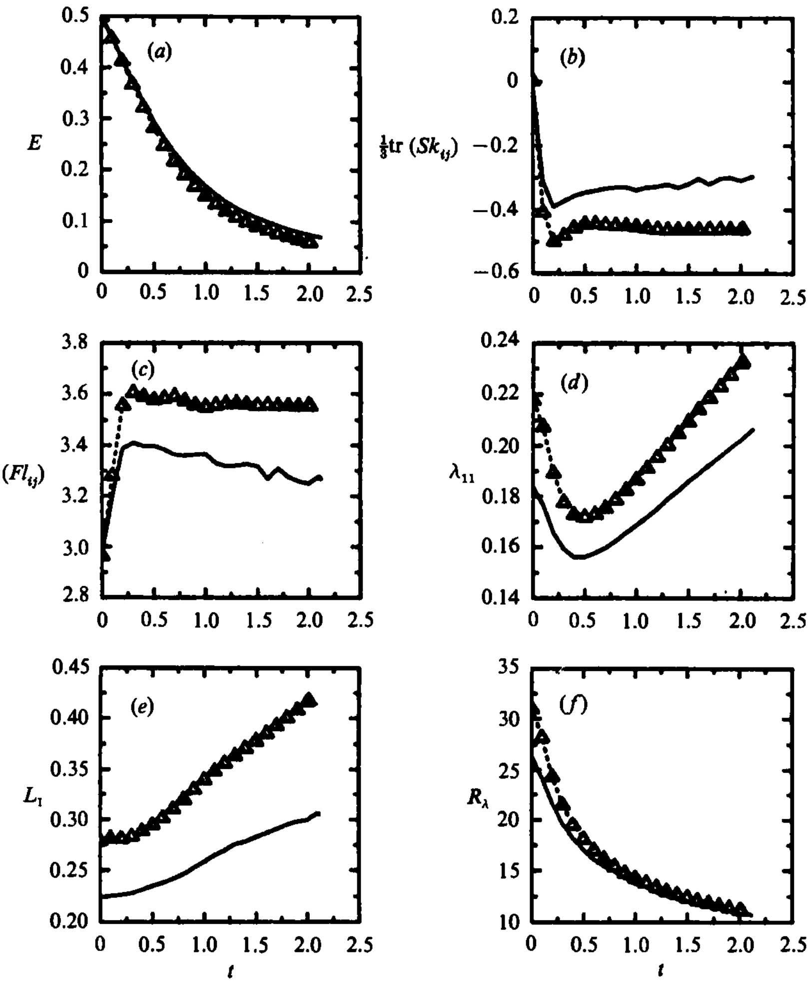

FIGURE 10. Turbulence statistics for 96^3 DNS at $t = 0.8$. Parameters are $k_0 = 10$, $\chi_0 = 0$ (Δ) and $\chi_0 = 0.2$ (—), $(M_t)_0 = 0.1$, $(\rho_{\mathrm{rms}})_0 = 0$, $(T_{\mathrm{rms}})_0 = 0.0626$, $Re = 250$. (a) $E = E^{\mathrm{C}} + E^{\mathrm{I}}$, (b) trace of skewness tensor, (c) trace of flatness tensor, (d) Taylor microscale, (e) integral lengthscale, (f) microscale Reynolds number.

These quantities represent a good choice of turbulence statistics to monitor the effects of compressibility.

In figure 13(a–f), a direct comparison of these statistics for the DNS and LES is made for a filter width $\Delta_f = 2$. It is clear that the LES does an excellent job in reproducing the results of the DNS, with the possible exception of χ. It should be noted that χ exhibits acoustic oscillations and hence is a difficult quantity to predict accurately; nonetheless, the LES yields results that are in good qualitative agreement with the direct simulation. The most striking result is how well the compressible turbulent kinetic energy and dilatational terms are captured.

It was found that a change in the filter width Δ_f to 1 or 3 – and an adjustment of the SGS model constants C_R and Pr_T of up to 25% – only led to a mild degradation of the results. However, the subgrid-scale models did play a crucial role in obtaining the accurate results shown in figure 13 (i.e. a 32^3 direct simulation is substantially under-resolved). To illustrate this point, the results of a direct simulation on the

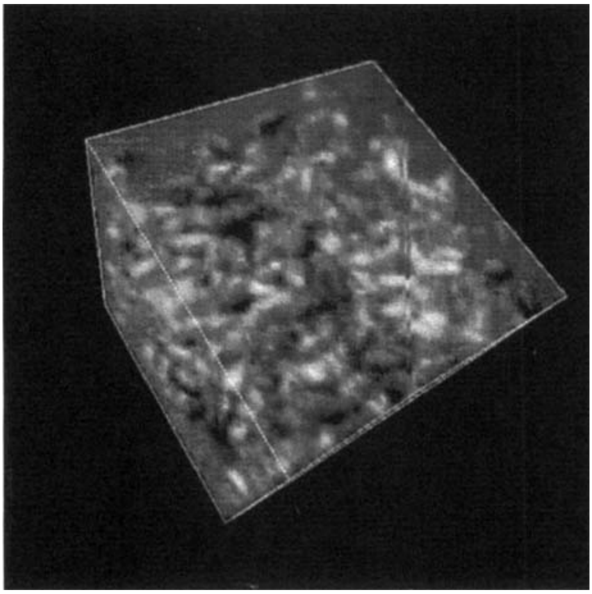

FIGURE 11. Volumetric representation of ω^2. Parameters are identical to those of figure 10.

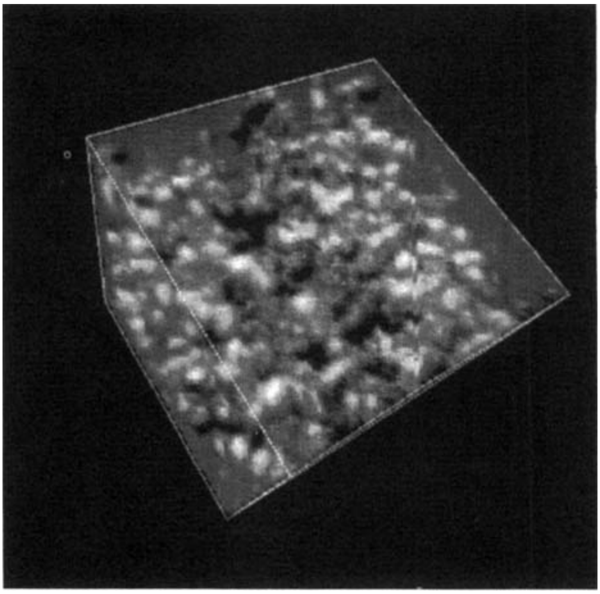

FIGURE 12. Volumetric representation of $(\nabla \cdot \boldsymbol{v})^2$. Parameters are identical to those of figure 10.

coarse 32^3 grid (i.e. an LES for $\Delta_f = 0$) is shown in figure 14 for the same test case. It is clear from this figure that the coarse grid DNS does a poor job in capturing the incompressible as well as the compressible turbulence statistics. Consequently, it is the adequate performance of the subgrid-scale models in draining the proper amount of energy from the filtered fields (to account for the presence of unresolved scales) which leads to the excellent results obtained in figure 13. Considering the degree of compressibility exhibited by the turbulence statistics for the test case considered in

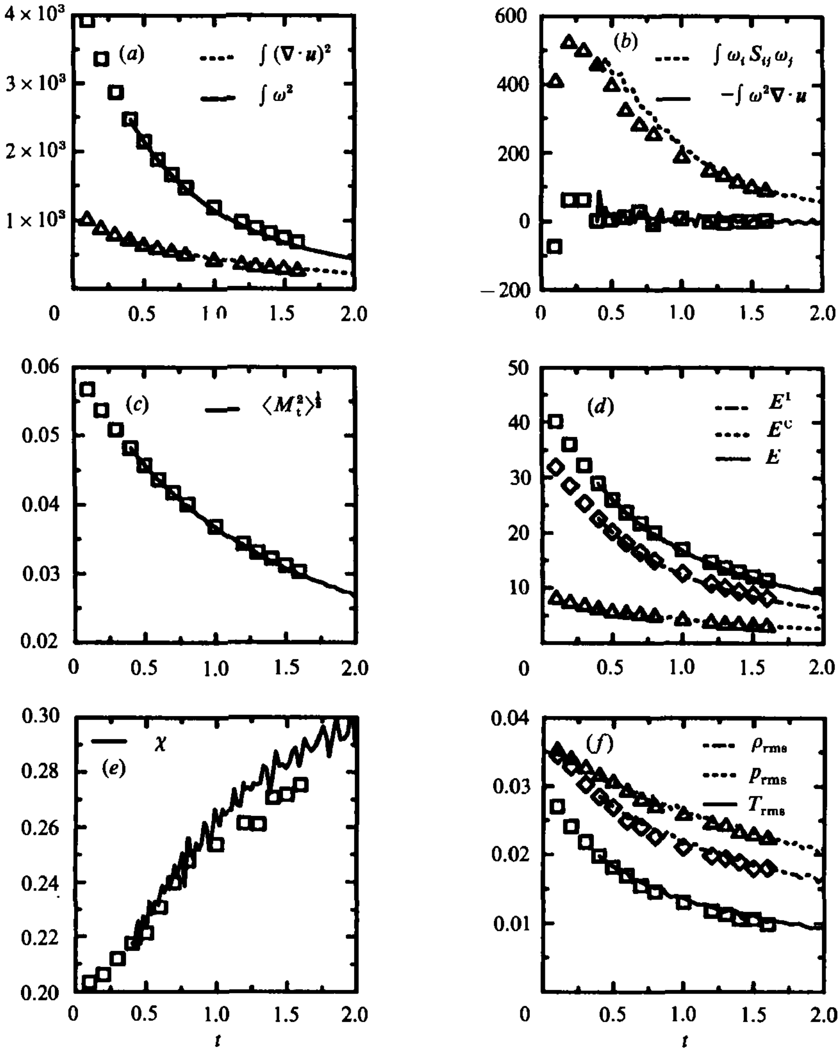

FIGURE 13. Comparison between LES results (—, -·-, - - -) and results from a 96^3 DNS (△, □, ◇) injected onto the 32^3 LES grid. Filter width $\Delta_c = \Delta_f = 2$.

this section, it would appear that the feasibility of the proposed subgrid-scale models has been established. A more extensive parametric study of this subgrid-scale model has been constructed recently by Zang *et al.* (1992).

7. Conclusion

New subgrid-scale models for compressible turbulence have been developed and tested against the results of direct numerical simulations of compressible isotropic turbulence. These compressible subgrid-scale models, which were based on the Favre-filtered equations of motion for an ideal gas, contain two dimensionless constants and reduce to the linear combination model of Bardina *et al.* (1983) in the incompressible, isothermal limit. The subgrid-scale stress model constant was found to assume the value of $C_R = 0.012$ which gives rise to correlations between the exact and modelled stresses that were above 70% on the tensor, vector and scalar levels

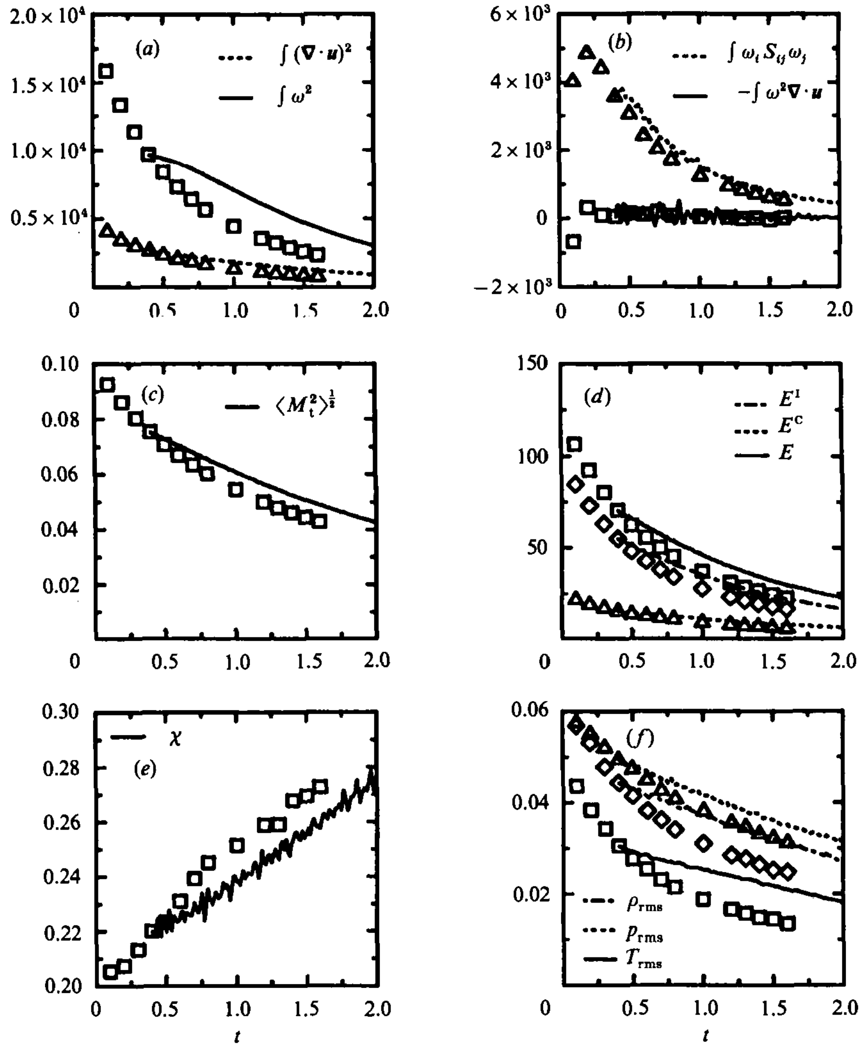

FIGURE 14. Same as figure 13 but for filter width $\Delta_c = \Delta_I = 0$.

– a correlation which compares favourably with those obtained in earlier work on the subgrid-scale modelling of incompressible turbulent flows. Another encouraging feature lies in the fact that these constants and their associated correlations were found to be comparatively insensitive to mean Mach numbers in the range $0 < M_0 < 0.6$.

The results from a coarse grid 32^3 LES of compressible isotropic turbulence conducted with the subgrid-scale models derived in this paper were shown to be in excellent agreement with those obtained from a 96^3 direct simulation. These results are extremely encouraging since, for the case considered, on average 25% of the turbulent kinetic energy was compressible. Furthermore, the ability for the LES to accurately capture the dilatational statistics of the flow was quite surprising.

Future research will be conducted on several fronts. The large-eddy simulation of a compressible turbulent flow with mean temperature gradients could lead to refinements in the subgrid-scale heat flux model. Furthermore, the large-eddy simulation of compressible, homogeneous shear flow could yield new insights into the performance of these subgrid-scale models. Near-wall modifications will also be implemented that allow for the large-eddy simulation of compressible, wall-bounded turbulent flows. While further improvements are still possible, we believe that the essential foundation for the large-eddy simulation of compressible turbulent flows has been established in this study. With future research, compressible LES could have a profound impact on the analysis of supersonic and hypersonic flows of aerodynamic importance.

This research was supported by the National Aeronautics and Space Administration under NASA Contract No. NAS1-18605 while G.E., M.Y.H. and C.G.S. were in residence at the Institute for Computer Applications in Science and Engineering (ICASE), NASA Langley Research Center, Hampton, VA 23665, USA.

Appendix

Initial energy spectrum

Both the incompressible and compressible direct simulations impose a specified energy spectrum on the initial random velocity distribution. For comparative purposes, the data was obtained from Comte-Bellot & Corrsin (1971). They tabulate the function $E_{11}(k)$ which is related to the energy spectrum $E(k)$ by

$$E(k) = \tfrac{1}{2}k^3 \frac{\mathrm{d}}{\mathrm{d}k}\left[\frac{1}{k}\frac{\mathrm{d}E_{11}}{\mathrm{d}k}\right]. \tag{A 1}$$

Unfortunately the data are noisy, so a least-squares fit is performed on $\log E_{11}$, expressed as a fourth-order polynomial in $\log k$. The final form obtained for E_{11} is

$$\log(E_{11}) = 2.64359 - 0.72602(\log k) - 0.32585(\log k)^2 + 0.03525(\log k)^3 - 0.02344(\log k)^4. \tag{A 2}$$

Calculation of model constants

Before correlating the total exact subgrid-scale stress against its model, the model constants must be determined. There are many ways of accomplishing this among which two are retained. The total modelled stress is written as a linear combination of the modelled terms $C_i \tau_i^{\mathrm{m}}$:

$$\tau^{\mathrm{m}} = \sum_{i=1}^{n} C_i \tau_i^{\mathrm{m}}, \tag{A 3}$$

while the exact total stress is simply

$$\tau^{\mathrm{e}} = \sum_{i=1}^{n} \tau_i^{\mathrm{e}}, \tag{A 4}$$

where superscripts m and e denote 'modelled' and 'exact' respectively. The unknown constants to be determined are the C_i. The first approach adopted is to calculate the root-mean square of the pairs $C_i \tau_i^{\mathrm{m}}$ and τ_i^{e} and equate them for each value of i. The constants thus take the values

$$C_i = \sigma_{\tau_i^{\mathrm{e}}} / \sigma_{\tau_i^{\mathrm{m}}}. \tag{A 5}$$

This method is referred to by RMS in the text.

A least-squares method applied to the total stress as a whole is an alternative approach. In this case, the norm

$$\|\tau^{\mathrm{m}}-\tau^{\mathrm{e}}\|^2 = \left\|\sum_{i=1}^{n}(\tau_i^{\mathrm{e}}-C_i\tau_i^{\mathrm{e}})\right\|^2 \tag{A 6}$$

is minimized with respect to the coefficients C_i. This gives rise to a linear system in the coefficients which can be solved by direct methods if the number of constants is not too large. For the subgrid-scale model considered in the text, $n = 3$.

Definitions

For reference purposes, several statistical definitions are provided here. All variables are defined on a three-dimensional grid and are subscripted by a single index i for convenience. The average of a function $\mathscr{F}_i$ is

$$\langle\mathscr{F}\rangle = \frac{1}{N}\sum_{i=1}^{N}\mathscr{F}_i. \tag{A 7}$$

As a function of the average, the r.m.s. of $\mathscr{F}$ is

$$\mathscr{F}_{\mathrm{rms}} = [\langle(\mathscr{F}-\langle\mathscr{F}\rangle)^2\rangle]^{\frac{1}{2}}. \tag{A 8}$$

Correlation coefficients are fundamental in evaluating subgrid-scale models. The correlation coefficient between two functions $\mathscr{F}$ and $\mathscr{G}$ is

$$C(\mathscr{F},\mathscr{G}) = \frac{\langle\mathscr{F}\mathscr{G}\rangle}{\mathscr{F}_{\mathrm{rms}}\,\mathscr{G}_{\mathrm{rms}}}. \tag{A 9}$$

REFERENCES

ABARBANEL, S., DUTT, P. & GOTTLIEB, D. 1989 Splitting methods for low Mach number Euler and Navier–Stokes equations. *Computers & Fluids* **17**, 1–12.

ARFKEN, G. 1970 *Mathematical Methods for Physicists*. Academic.

BARDINA, J., FERZIGER, J. H. & REYNOLDS, W. C. 1983 Improved subgrid-scale models based on large-eddy simulation of homogeneous, incompressible, turbulent flows. *Stanford University Rep.* TF-19.

BATCHELOR, G. K. 1967 *An Introduction to Fluid Dynamics*. Cambridge University Press.

BIRINGEN, S. & REYNOLDS, W. C. 1981 Large-eddy simulation of the shear-free turbulent boundary layer. *J. Fluid Mech.* **103**, 53–63.

BLAISDELL, G. A., MANSOUR, N. N. & REYNOLDS, W. C. 1991 Numerical Simulations of Compressible Homogeneous Turbulence. *Stanford University Rep.* TF-50.

CANUTO, C., HUSSAINI, M. Y., QUARTERONI, A. & ZANG, T. A. 1988 *Spectral Methods in Fluid Dynamics*. Springer.

CLARK, R. A., FERZIGER, J. H. & REYNOLDS, W. C. 1979 Evaluation of subgrid-scale models using an accurately simulated turbulent flow. *J. Fluid Mech.* **91**, 1–16.

COMTE-BELLOT, G. & CORRSIN, S. 1971 Simple Eulerian time correlation of full and narrow-band velocity signals in grid-generated, isotropic turbulence. *J. Fluid Mech.* **48**, 273–337 (referred to herein as CBC).

DEARDORFF, J. W. 1970 A numerical study of three-dimensional turbulent channel flow at large Reynolds numbers. *J. Fluid Mech.* **41**, 453–480.

EIDSON, T. M. 1985 Numerical simulation of the turbulent Rayleigh–Bénard problem using numerical subgrid modeling. *J. Fluid Mech.* **158**, 245–268.

ERLEBACHER, G., HUSSAINI, M. Y., KREISS, H. O. & SARKAR, S. 1990 The analysis and simulation of compressible turbulence. *Theor. Comput. Fluid Dyn.* **2**, 73–95.

FEIEREISEN, W. J., REYNOLDS, W. C. & FERZIGER, J. H. 1981 Numerical simulation of compressible, homogeneous, turbulent shear flow. *Stanford University Rep.* TF-13.

FRISCH, U. & ORSZAG, S. A. 1990 Turbulence: challenges for theory and experiment. *Phys. Today* **43**, 24–32.

HINZE, J. O. 1975 *Turbulence.* McGraw-Hill.

HUSSAINI, M. Y., SPEZIALE, C. G. & ZANG, T. A. 1990 Comment on the potential and limations of direct and large-eddy simulations. In *Lecture Notes in Physics*, vol. **357** (ed. J. L. Lumley), pp. 354–368.

HUSSAINI, M. Y. & ZANG, T. A. 1987 Spectral methods in fluid dynamics. *Ann. Rev. Fluid Mech.* **19**, 339–368.

KERR, R. M. 1985 Higher-order derivative correlations and the alignment of small-scale structures in isotropic, numerical turbulence. *J. Fluid Mech.* **153**, 31–58.

LEONARD, A. 1974 On the energy cascade in large-eddy simulations of turbulent fluid flows. *Adv. Geophys.* **18**, 237–248.

LUMLEY, J. L. 1983 Turbulence modeling. *Trans. ASME* E: *J. Appl. Mech.* **50**, 1097–1103.

MCMILLAN, O. J. 1980 Tests of new subgrid-scale models in strained turbulence. *AIAA Paper* 80–1339; in *AIAA 13th Fluid and Plasma Dynamics Conf. Snowmass, CO.*

MCMILLAN, O. J. & FERZIGER, J. H. 1979 Direct testing of subgrid-scale models. *AIAA J.* **17**, 1340–1346.

PASSOT, T. & POUQUET, A. 1987 Numerical simulation of compressible homogeneous flows in the turbulent regime. *J. Fluid Mech.* **181**, 441–466.

PIOMELLI, U., FERZIGER, J. H. & MOIN, P. 1987 Models for large-eddy simulations of turbulent channel flows including transpiration. *Stanford University Tech. Rep.* TF-32.

PIOMELLI, U., ZANG, T. A., SPEZIALE, C. G. & HUSSAINI, M. Y. 1990 On the large-eddy simulation of transitional wall-bounded flows. *Phys. Fluids* A **2**, 257–265.

REYNOLDS, W. C. 1976 Computation of turbulent flows. *Ann. Rev. Fluid Mech.* **8**, 183–208.

ROGALLO, R. S. & MOIN, P. 1984 Numerical simulation of turbulent flows. *Ann. Rev. Fluid Mech.* **16**, 99–137.

SARKAR, S., ERLEBACHER, G., HUSSAINI, M. Y. & KREISS, H. O. 1991 The analysis and modeling of dilatational terms in compressible turbulence. *J. Fluid Mech.* **227**, 473–493.

SCHUMANN, U. 1975 Subgrid scale models for finite difference simulations of turbulent flows in plane channels and annuli. *J. Comput. Phys.* **18**, 376–404.

SPEZIALE, C. G. 1985 Galilean invariance of subgrid-scale stress models in the large-eddy simulation of turbulence. *J. Fluid Mech.* **156**, 52–62.

SPEZIALE, C. G., ERLEBACHER, G., ZANG, T. A. & HUSSAINI, M. Y. 1988 The subgrid-scale modeling of compressible turbulence. *Phys. Fluids* **31**, 940–942.

TENNEKES, H. & LUMLEY, J. L. 1972. *A First Course in Turbulence.* MIT Press.

VOKE, P. R. & COLLINS, M. W. 1983 Large-eddy simulation: retrospect and prospect. *PhysicoChem. Hydrodyn.* **4**, 119–161.

YOSHIZAWA, A. 1986 Statistical theory for compressible turbulent shear flows, with the application to subgrid modeling. *Phys. Fluids* **29**, 2152–2164.

ZANG, T. A., DAHLBURG, R. B. & DAHLBURG, J. P. 1992 Direct and large-eddy simulations of compressible Navier–Stokes turbulence. *Phys. Fluids* A **4**, 127–140.